POLITECNICO DI TORINO

Department of Mechanical and Aerospace Engineering

Master of Science in Mechanical Engineering

Dynamic design of electric turbo-compound

Supervisor: Prof. Nicola AMATI

Co-supervisor: Prof. Andrea TONOLI

Ph.D. Renato GALLUZZI

Dott. Salvatore CIRCOSTA

Candidate:

DAVIDE SCIPIONI

Identification number: 252824

Academic Year 2018-2019

Keep your eyes on the stars, and your feet on the ground

Theodore Roosevelt

Ringraziamenti

Vorrei innanzitutto ringraziare il Professor Nicola Amati, che mi ha seguito in questo percorso, ed ha reso possibile questo lavoro di tesi. Un ringraziamento particolare va a Salvatore che mi ha seguito, con la sua infinita disponibilità, in ogni step della realizzazione dell'elaborato.

E poi, ovviamente, non posso non ringraziare la mia famiglia, senza la quale non avrei potuto intraprendere questo percorso, grazie per avermi sopportato in questi mesi.

Grazie ai miei amici, Eleonora, Gabriele, Mirna, Nicolò, per essere stati sempre presenti anche durante questa ultima fase del mio percorso di studi. Grazie per aver ascoltato i miei sfoghi, grazie per tutti i momenti di spensieratezza.

Un ringraziamento speciale a Sara, mia fonte d'ispirazione, per avermi trasmesso la sua immensa forza e il suo coraggio. Grazie per tutto il tempo che mi hai dedicato. Grazie perché ci sei sempre stata.

Abstract

Electric turbo-compounding is gaining popularity among hybrid vehicles. This device is composed of an electric machine - mounted on the shaft between the turbine and the compressor - that can operate both as a motor and as a generator. This allows recovering part of the thermal energy that otherwise would be discharged at the exhaust. In this way, the drivability and fuel consumption are improved. In this context, the *Research Unit High Efficiency Hybrid Powertrain* has been founded to develop new components to increase the efficiency of hybrid vehicles. Politecnico di Torino has been involved to study and design a prototype of a high-speed hysteresis machine for an electric turbo-compound. In the mechanical design of a high-speed electric machine different aspects must be considered: the machine works at 150000 rpm, and at this speed issues like vibration linked with rotordynamic and rotor failure because of high centrifugal forces may arise. To address these aspects, the present thesis deals with the mechanical design and dynamic investigation of the electric machine rotor to prevent the aforementioned problems. In the first part, tensile tests are conducted to identify the mechanical properties of different semi-hard magnetic materials. This step allowed the selection the material suitable for the realization of the rotor. From this analysis, the CROVAC results to be the best for this application. Subsequently, a finite element analysis is carried out to study the dynamics of the rotor. The comparison between experimental data and analytical models of the free-free rotor is proposed: this allows tuning the parameters to have an accurate finite element model. Finally, an appropriate analysis of the O-Rings used to support the shaft is carried out so that the critical speeds and unbalance response can be computed. The satisfying numerical results of the supported rotor allow moving on the experimental tests at a high rotational speed. These tests are successfully conducted, and they have confirmed the proper functioning of the rotor and the goodness of the design and assemble. Thus, these analyses have allowed to obtain an experimentally validated finite element model for the free-free rotor, and from the high-speed experimental test the waterfall diagram is got: the first critical speed is very close to the predicted one.

Contents

List of Figures

List of Tables

Chapter 1

Introduction

1.1 Thesis motivation

Nowadays, the toxic emissions of cars in the urban area are one of the most important environmental problem. The EU commission estimates that the cars are responsible for the 20% of the whole toxic emission. To solve this problem the EU parliament in 2019 agreed on reducing the average CO_2 emissions for passenger cars by 15% in 2025 and by 37,5% in 2030 with respect to the 95 g/km of the 2020 regulation [1]. These new targets are the most ambitious in the world (see Figure 1.1).

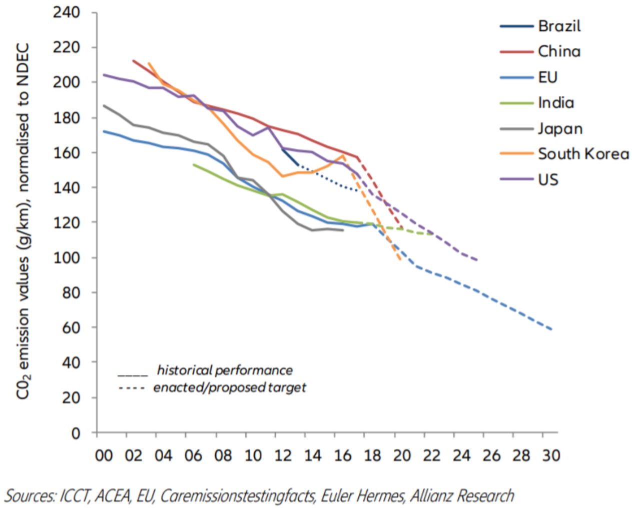

Figure 1.1: *Passenger car CO_2 emissions*

CO_2 emissions are closely linked to vehicle efficiency. Different solutions have been tested during the years to try improving the vehicle efficiency. Among the proposed solutions, the most successful one are certainly solutions involving the use of electric machines aimed at recover energy from different sources. Bearing this scenario in mind, the efforts of car manufacturers must aim towards more efficient electric drive systems.

1.2 Power recovering systems in automotive

Several solutions have been developed to try recovering power from various sources, in order to increase the efficiency and reduce the fuel consumption. The ICE is undoubtedly the main source of power loss in a vehicle, it is estimated that only 30% of the input power is converted into mechanical power [2]. However, there are other sources from which power can be recovered, for example from road vibrations through the use of regenerative suspensions. The figure 1.2 shows the most common solutions for power recovery in automotive systems.

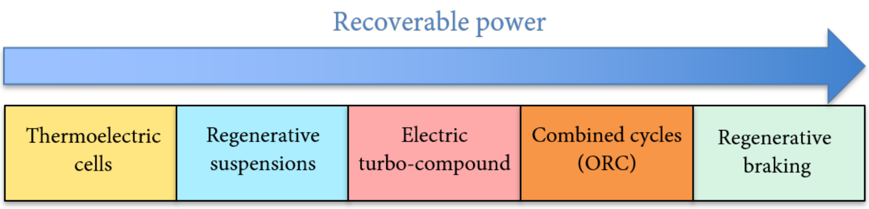

Figure 1.2: *Power recovery in automotive*

The system of thermoelectric cells consists of generating electricity using the heat from the exhaust gases. The principle of electricity production is based on the Peltier-Seebeck effect, and the electrical current is produced by the temperature difference between the exhaust gases and the surface of the electrical generator. The maximum generated power is about 300 W [3].

The regenerative suspensions allow recovering energy from the vibrations induced by the road surface. In particular, the fundamental role is played by the damper, which commonly dissipates vibrating energy coming from the road into heat. In regenerative suspensions the damper will transform the kinetic energy into electricity and store it for late use. The maximum generated power is up to 400-500 W [4]. These types of suspension, with an active control of the damping, increase the ride comfort [2].

The regenerative braking is one of the most diffuses solutions in hybrid vehicles. It consists in converting the kinetic energy of the vehicles, that would be otherwise lost by the brake discs as heat, into electricity. The maximum generated electric power is 60 kW [5].

The Organic Rankine Cycle (ORC) is another solution aimed at recovering energy from the exhaust and transform it into electricity. It consists in using the exhaust gases to heat up an organic fluid that expands itself into a turbine generating electricity. The results in terms of energy recovery are good, but the design and the management of this system is complex, discouraging the use.

One of the most challenging but effective solution for traditional and hybrid powertrain is the use of electric turbo-compound. Electric turbo-compounding is a technology used to extract electric energy from the exhaust gases of an internal combustion engine. In these systems, when the power given by the turbine exceeds the one required by the compressor, the power surplus is converted into electrical energy and it is stored.

Its design is relatively simple and in [6] it is shown that this device can provide the same benefits (in terms of fuel economy and car drivability) of an hybrid architecture in which the electric motor is directly connected to the crank-shaft. [7] shows that this device can increase the power of the ICE of 11 kW. Garrett [8], that will launch his electric turbo-compound in 2021, has confirmed an increase of the performance in terms of torque of 10% and a decrease of the fuel consumption between 2% and 4%.

1.3 Electric turbo-compounding

There are mainly two types of electric turbo-compounding systems for internal combustion engine: the first, shown in figure 1.3, is composed by a power turbine in series with the turbocharger to recover the extra energy downstream the compressor; the second configuration, shown in figure 1.4, is composed by the electric machine mounted on the same shaft of both the compressor and the turbine to recover the energy surplus in the turbine.

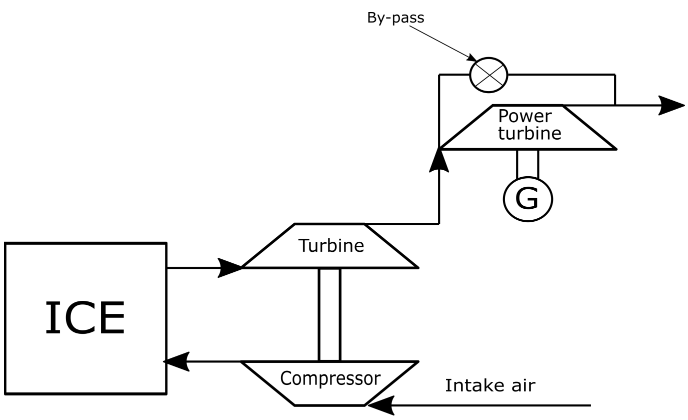

Figure 1.3: *Electric turbo-compound with power turbine*

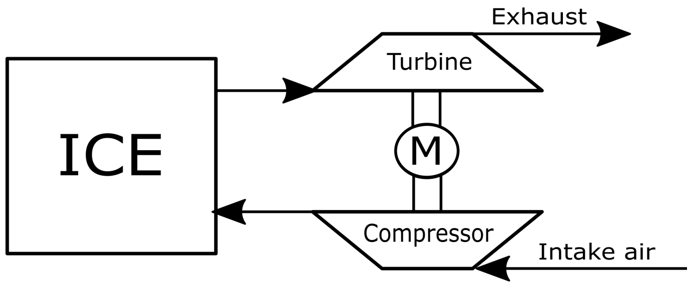

Figure 1.4: *Electric turbo-compressor*

In the first configuration the electric motor works only as generator, so the stored energy will be used for other tasks, like giving power to an electric motor mounted on the engine flywheel.

In the second configuration, the electric machine can work both as motor and as generator. In particular, when the exhaust gases do not have enough energy or a rapid acceleration of the shaft is required, the electric machine works as a motor, supplying the power required. This give the opportunity to use the electric motor in order to reduce the turbo-lag, that is one of the main problem of the mechanic turbo-compressors.

Thus, on one hand the main advantage of the electric turbo-compound is the fact that they permit to control the rotational speed of the turbine, in such a way to optimize the efficiency at each angular speed of the motor. On the other hand, they increase the back-pressure in the exhaust manifold, generating an increasing of the fuel consumption. So, a trade-off between an increase in power and an increase of fuel consumption must be found.

In this thesis it has been analysed a prototype of an hysteresis electric machine that will be mounted between the compressor and the turbine, realizing an electric turbo-compound in the second configurations.

1.3.1 Design requirements for electric turbo-compound

In the design of an electric turbo-compound the main aspects that have to be analysed are the following [9]:

- *Mechanical strength* has a key role because the maximum rotational speed is proportional to the material tensile strength, and usually the rotation speed of electric turbo-compound is up to 180 krpm [6].

- *Rotordynamics* is another important issue since the rotor may cross one of more critical speed during its acceleration. The main aspects of the rotordynamics are the non-rotating damping and the presence of an unbalanced magnetic force. The first is fundamental to reduce the displacement of the rotor while the latter can have an important effect on the values of the critical speeds. In fact the resultant attractive force between the rotor and the stator appears as a negative stiffness, causing a reduction of the critical speeds [10].

- *Thermal behaviour* is a common problem in electric turbochargers because of the high temperature of the exhaust gases.

- *Output power density* is a key aspect, especially in the automotive field in which compactness and lightness are fundamental requirements. So an electrical machine with high output power density is recommended.

1.3.2 Electric machine in turbo-compounding

In literature, the most common electric machines used in electric turbo-compounds are permanent-magnet (PM), switched reluctance machines (SRM) and asynchronous induction machines. An interesting discussion about the main advantages and disadvantages of the aforementioned machines, with reference to electric turbocharging, has been done by Bumby et al. [11].

The permanent-magnet machines are recognized as favoured in electric turbocharging due to their high power density, high efficiency and relatively simple construction. However, the PM machines are approaching their limits [10]. The first limit is a thermal one: an high working temperature (220 °C for NdFeB and 350 °C for SmCo) can cause the demagnetization of the rotor. Other limits of the PM machine are connected to mechanical and rotordynamic aspects. The mechanical strength of the material is proportional to the maximum reachable spinning speed, and usually a rigid sleeve on the rotor is necessary to avoid the magnet detachment at high speed. The sleeve increases the air-gap of the electric motor reducing the output power density. Regarding the rotordynamic, Borisavljevic et al. underline how the first flexural critical speed often represents the stability limit of the rotor [10].

The asynchronous machine is widely used and some examples can be found in literature [12], [13]. However, in [11] some problems are reported. Despite their robustness, this type of electric machine suffer the rotor high temperature and for this an intensive cooling is required. A particular type of asynchronous machine that represents a valid alternative for its small volume is the axial flux machine. The main drawback of this machine is that the conventional PWM control technique cannot be used [11].

The switched reluctance machine is also an alternative for electric turbo charging and some example of application can be found in [14] and in [15]. The drawbacks of this electric machine are linked to the large air-gap and to the necessity of having a large inverter in order to compensate the high input current demand [11].

Another type of electric machine not so much studied for these types of applications is the hysteresis machine. Galluzzi et al. [9] make an interesting feasibility study for the application of the hysteresis machine in the electric turbocharger, with a particular focus on the comparison between the mechanical and the thermal behaviour of the material used for the hysteresis machine (SHMMs) and the permanent magnets. In Figure 1.5 this comparison is reported.

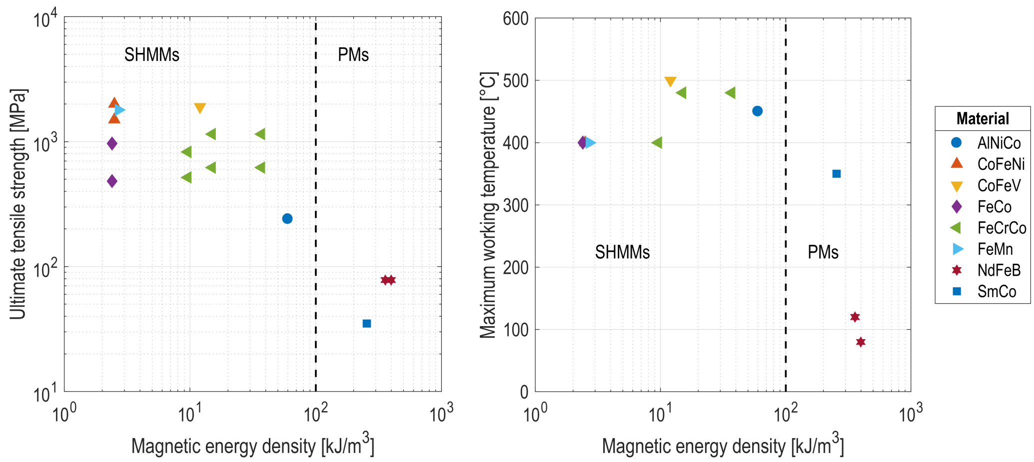

(a) *UTS vs magnetic energy density*

(b) *Maximum T vs magnetic energy density*

Figure 1.5: *SHMM and PM material comparison [9]*

The SHMMs used in the hysteresis electric machine have a mechanical resistance higher than the one of the material used in the PM machine. This means that with the hysteresis motor is possible to reach higher rotational speed. Moreover, the SHMMs show an higher working temperature with respect to the material used in PM electric machine.

The high speed and the high working temperature are two of the most critical factors in electric turbocharger, so the hysteresis electric machine seems a suitable solution for electric turbo-compound. However, it must be noted that they are characterized by low magnetic energy density [16], and this is a negative aspect for electric turbo-compound, in which the compactness is a key factor. However, this aspect is compensated by the higher angular speed that can be reached with a hysteresis machine.

1.4 Hysteresis electric machine

Hysteresis motors are first described by Steinmetz in 1917 [17]. They are known as self-starting motor with the ability of producing uniform torque from rest to synchronous speed [18].

Nowadays, the hysteresis machines are used in low-speed and niche applications, like gyroscope, clocks and low-power precision equipment [18]. They are also used to realize clutches and couplers but also in textile and paper industrial plants [19].

They have a simple structure with a conventional stator and a solid rotor composed of a material having a high degree of magnetic hysteresis, usually semi-hard magnetic material (SHMM). In particular, two different configurations of hysteresis machine can be found in literature [16]:

- *Cylindrical hysteresis machines* have a cylindrical rotor made of hysteretic material (Figure 1.6). The rotor is surrounded by the stator in two possible configurations [18]:
  - *Inner-rotor*: the rotor is mounted inside the stator windings
  - *Outer-rotor*: the rotor is mounted outside the stator windings: this solution is more compact than the inner-rotor one.

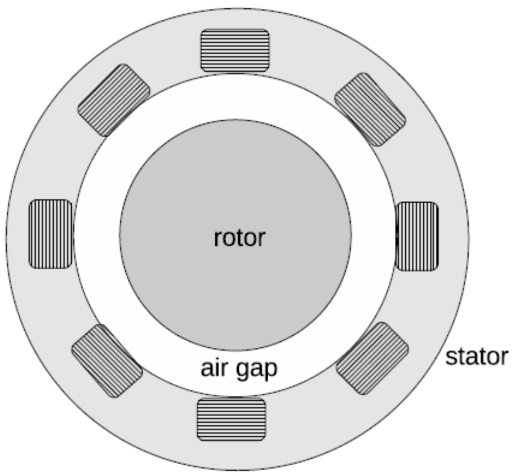

Figure 1.6: *Cross-sectional view of an inner-rotor cylindrical hysteresis machine [16]*

- *Disks hysteresis machines* have an annular ring rotor (Figure 1.7). Among this type of hysteresis machines is possible to distinguish:

- *Circumferential-field hysteresis machines* have a ring support made with a material that has a low magnetic permeability. Thanks to this ring the magnetic field lines in the rotor are mostly circumferential to the ring.
- *Axial-field hysteresis machines* have a ring support made with a material that has an high magnetic permeability. If the ring is thin, the magnetic field lines in rotor are mostly axial.

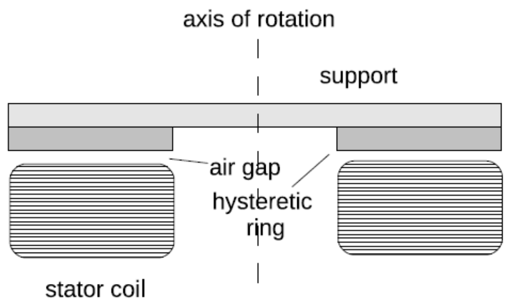

Figure 1.7: *Cross-sectional view of a disk hysteresis machine [16]*

These types of machines exploit the principle of magnetic hysteresis to produce power: the energy wasted in magnetic hysteresis is converted into mechanical energy. When an external magnetic field (**H**) is applied to a virgin ferromagnetic material, this becomes magnetized (**B**) in the direction of **H**, following the first magnetization curve. This curve increases rapidly at first and then approaches an asymptote called magnetic saturation. If the external magnetic field is reduced, the material demagnetize following a different path, and when the external magnetic field becomes nil, the material remains magnetized. This residual magnetization can be removed by applying a coercitive field in the opposite direction. If the value of H increases in this direction, the negative saturation value is reached. Starting from this and increasing the external field H it is possible to close the loop shown in Figure 1.8.

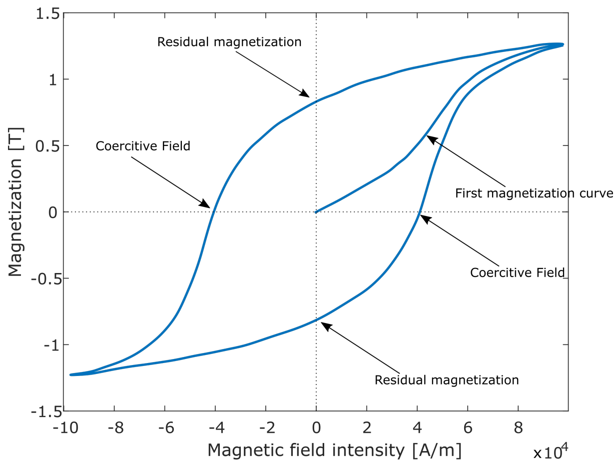

Figure 1.8: *Magnetic hysteresis loop*

When supply is given to the stator, a rotating magnetic field is produced. This rotating field creates poles on the rotor, that follow the statoric rotating field and pull the rotor along. Because of the magnetic hysteresis loss in the rotor, the axis of the rotor field and the one of the stator field are misaligned by an angle δ (see Figure 1.9), that is load dependent. This angle is the responsible for the torque production [16].

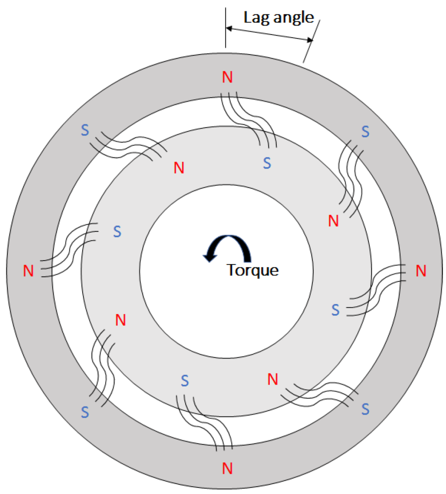

Figure 1.9: *Lag angle*

The maximum torque of the hysteresis motor (pull-out torque) is proportional to the hysteresis loop amplitude [18].

Two different operation modes of the hysteresis machine can be distinguished:

- *Asynchronous operation*: The machine works in this condition during the speed-up and when the load torque is higher than the maximum torque . The rotational speed of the machine is lower than the stator field's frequency and the machine slips.

- *Synchronous operation*: The machine works in this condition when the load torque is equal or less than the maximum torque. The machine rotates at the same frequency of the stator magnetic field;

Generally, the hysteresis machines are designed to work in synchronous operation. In this mode the hysteresis loop is no longer done and the machine works like a permanent magnet motor: the torque is load dependent [16]. However, during the speed-up, the machine works in asynchronous operation until the synchronous speed is reached. In this phase the torque is constant and equal to the pull-out value, so the hysteresis machine work as an induction motor in asynchronous operation [16].

The performance of hysteresis machines is strictly related to the magnetic material that has to ensure good mechanical resistance to guarantee, high speed and large hysteresis loop to transmit torque. Generally all the metallic materials are subjected to magnetic hysteresis, among them a particular compromise between mechanical and magnetic properties can be found in semi-hard magnetic material (SHMM).

1.5 Thesis objective

The present thesis arose from the needed to develop new components to increase the efficiency of hybrid vehicles, increasing the energy recovering from different sources. In this context, the *Research Unit High Efficiency Hybrid Powertrain* has been founded, and in particular, Politecnico di Torino has been involved to study and design a prototype of a high-speed hysteresis machine for an electric turbo-compound.

The aim of this thesis is to design and analyse the dynamic behaviour of the rotor of an hysteresis machine for electric turbo-compound that has to reach 150000 rpm. At that speed issues like vibration, linked with rotordynamic, and rotor failure due to high centrifugal forces may arise. This analysis is aimed at preventing these problems. In order to achieve this aim, firstly the hysteresis material of the rotor has been experimentally characterized through a tensile test. This allows to design the rotor in such a way that it can withstand high rotational speed. Thus, the rotor has been realized by gluing 100 sheets of CROVAC. After that, a FEM rotordynamic analysis has been performed. Firstly a free-free rotor model of the shaft has been realized and validated in order to obtain the rotor properties without considering the supports. Then an analysis of the supports has been performed focusing on the O-Rings' behaviour. Their dynamic behaviour has been described with a Maxwell-Wiechert model whose parameters have been found through a genetic algorithm. At that point both the dynamic of the shaft and of the o-rings are determined, so they are coupled in order to find the critical speeds, poles map and unbalance response. Finally, rotor balancing and high speed experimental tests have been performed: they allow to demonstrate that the hysteresis machine can work at high speed, so that it can be used for a future application in electric turbocompound.

1.6 Thesis organization

The thesis is organized as follows:

- *Chapter 2*: It presents the experimental results of tensile tests on two different types of semi-hard magnetic material. Then, the rotor design and manufacturing are presented.
- *Chapter 3*: It proposes the rotordynamic model and validation of the free-free rotor.
- *Chapter 4*: The supports' dynamic is analysed and it is represented through a Maxwell-Wiechert model. A genetic algorithm has been used to identify the parameters of the Maxwell-Wiechert model. Thus, the supports' dynamic is coupled with the free-free dynamic model of the rotor, and the poles map, critical speeds and unbalance response is determined. Finally, the experimental test and the rotor balancing procedure are described.
- *Chapter 5*: In the final chapter conclusion and future works are reported.

Chapter 2

Hysteresis Rotor Design

In this chapter, the mechanical characteristics of different SHMMs have been analysed, focusing on CROVAC and on FeCrCo. On these materials the tensile test has been performed in order to determine the mechanical properties. In particular when CROVAC is considered, also the effect of heat treatment, needed to enhance its magnetic properties, is analysed.

Then, the rotor has been designed according to the high centrifugal forces. Particularly, being the internal diameter and the length of the rotor already fixed, only the external diameter must be determined with this analysis. Finally, the rotor has been realized in the LIM, and the process is described at the end of this chapter.

2.1 SHMM in electric machinery

Semi-hard magnetic materials are a set of materials characterized by modest coercivity and a good ductility. For that reason, they are capable of being formed and machined with standards metal-working tools.

The production of that material started in 1930 with the AlNiCo. Subsequently, other types of semi-hard magnetic materials like, FeCrCo, Arnokrome and Magnetoflex, were introduced. All these materials are characterized by the presence of cobalt, that increases the ductility of the materials but at the same time reduces their magnetic properties. To enhance the magnetic properties it is necessary a heat treatment: usually it consists of an annealing process for 3 hours at 500-570 °C. At that temperature there is recrystallization and grain growth: these aspects make the material brittle and with less ductility. Thus, the machining processes must be performed before the heat treatment. The main problem of these materials is the high cost due to the presence of Co.

In a first approach, the FeCrCo has been selected as the rotor's material. The mechanical characterization of this material, previously made in LIM, shows a very poor mechanical resistance: the specimen breaks at 2 MPa. In Figure 2.1 is shown a magnification of the FeCrCo48/5 broken specimen.

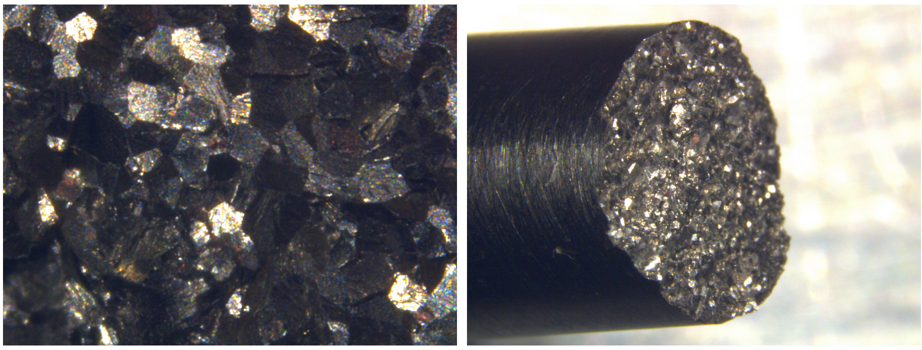

(a) **(b)**

Figure 2.1: *Tensile test of a FeCrCo48/5 specimen*

The fracture is clearly brittle: the surface is very shine and the crack is perpendicular to the direction of applied load. This confirms what it is previously introduced: on one hand the heat treatment enhances the magnetic properties but on the other hand the ductility reduces.

However, the measured tensile strength does not indicate the real resistance of the material. In fact, the sample has been supplied in the form of bulk material with a diameter of 35 mm, this diameter is sufficient to have the formation of pre-stress inside the material due to the heat treatment. For this reason, the SHMMs' specimen must be supplied as laminated: the laminated material, being thin, does not present problems of resistance related to heat treatment. Thus, if a thin material is considered the resistance is not a function of the specimen geometry, as happen in this case.

Because of these results, another material with higher mechanical resistance has been considered. In particular the focus has been put on CROVAC. The latter is a particular type of material with a low percentage of Co and a high percentage of Cr. It is produced by VACUUMSCHMELZE GmbH and, in order to compensate the absence of Co in terms of magnetic properties, it is subjected to a secret heat treatment.

The goal of this part is to find out the mechanical characteristics of the CROVAC, highlighting also the heat treatment effects on them. To accomplish this task, the tensile test is performed on a set of 10 specimens (5 before and 5 after the heat treatment), according to the ISO 6892-1.2016.

2.1.1 ISO 6892-1.2016

ISO 6892-1 measures the mechanical properties of metallic materials in any form at ambient temperature. The tests have been carried out at a controlled temperature of 23 degrees Celsius plus or minus 5 degrees. The most common mechanical properties measured with ISO 6892-1.2016 are the following:

1. *Yield Strength*: the stress at which a material becomes permanently deformed. ISO 6892-1.2016 specifies both upper and lower yield strength requirements for discontinuously yielding material (Figure 2.2a) and the offset yield method for continuously-yielding material (Figure 2.2b). In the case of discontinuous yielding

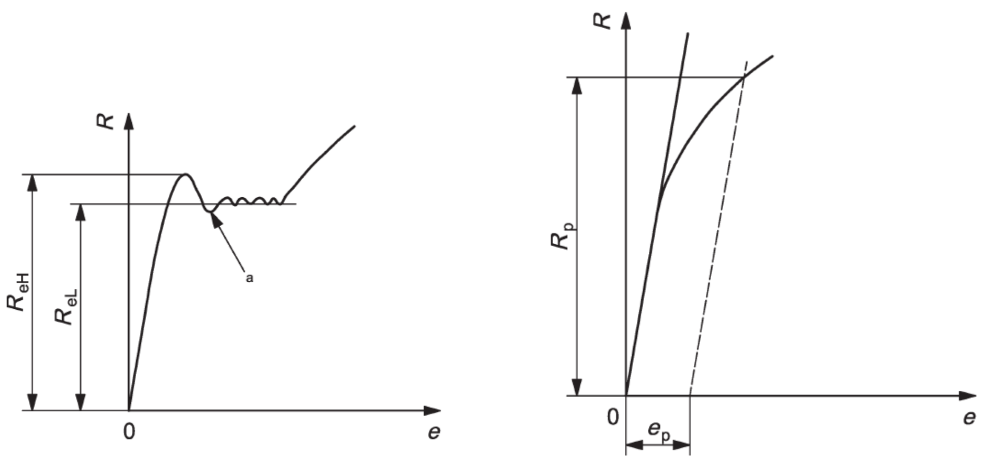

(a) *Discontinuous yielding* **(b)** *Continuous yielding*

Figure 2.2: *Yelding types*

   the upper yield strength is defined as the maximum value of stress prior to the first decade in force while the lower yield strength is the lowest value of stress during plastic yielding, ignoring any initial transient effect. In case of continuous yielding it is not possible to define an upper and a lower yield strength. The yield strength is defined as the value of stress for which there is a plastic deformation of the specimen of 0.2%;

2. *Tensile Strength*: stress corresponding to the maximum force;

3. *Percentage total extension at maximum force*: total extension (elastic plus plastic) at the moment of fracture. It is a measurement of the material's ductility;

4. *Modulus of elasticity*: stress rate of change (ΔR) with respect to the rate of

deformation (Δe) in the range of evaluation, expressed in percentage:

$$E = \frac{\Delta R}{\Delta e} \times 100 \tag{2.1}$$

ISO 6892—1 accommodates a wide variety of specimen types due to the huge range of applications of metallic materials. Primary specimen types include sheets, plates, wires, bars, and tubes.

In accordance with ISO 7500—1, the machine used for the test is of class 1 and it is able to produce a maximum force of 100 kN. The extensometer used for this test belongs to class 0.5, in accordance with ISO-9513, this class of extensometer is the one needed to find the modulus of elasticity.

2.1.2 CROVAC experimental results

The tensile test is performed on a set of 10 specimens, 5 are made of the not heat-treated material while the other 5 are heat-treated material. In this way it is possible to highlight the heat-treatment effect on the mechanical properties. In the tests the quantities that are directly measured are listed below:

1. *Force*: directly measured from the machine;
2. *Deformation*: measure with a class 0.5 extensometer,
3. *Displacement of the gripper* directly measured from the machine.

In post-processing, the tensile strength, the yield strength, the total extension at maximum force and the modulus of elasticity have been computed for each specimen. Finally, a normal distribution of each quantity is considered to characterize the material. This distribution has a 95% level of confidence. So, at the end of the post-processing all the aforementioned properties will be known in terms of average values and standard deviation and in the 95% of the case the property's value is inside the found interval.

The specimens used in the tensile test are sheets and the dimensions are reported in Figure 2.3.

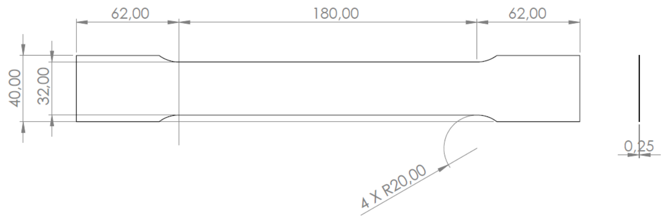

Figure 2.3: *CROVAC specimen*

The direct acquisition from the machine brings to the gripper displacement(C)-force(F) graph (Figure 2.4).

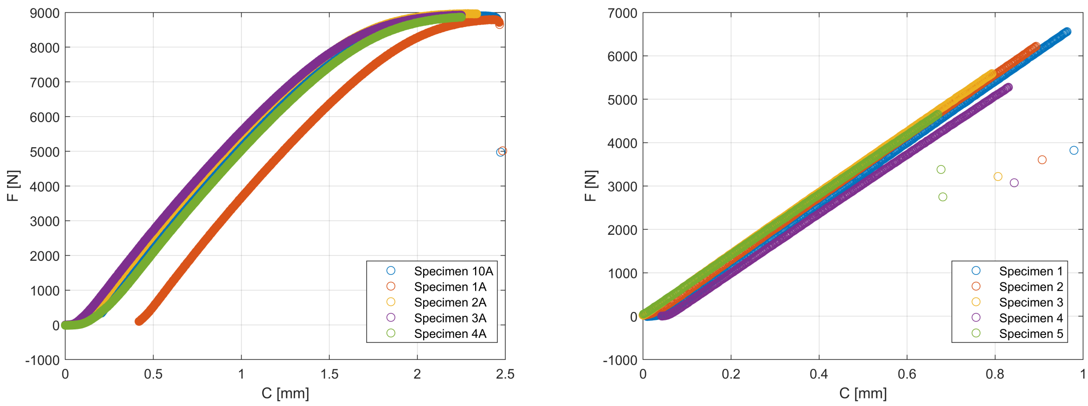

(a) *Non-treated specimen* **(b)** *Treated specimen*

Figure 2.4: *Force vs. gripper displacement curve*

By the measurement of the force (F) the normal stress can be calculated from Equation 2.2:

$$R = \frac{F}{A} \tag{2.2}$$

where A is the cross-section of the specimen.

Reporting in the same graph stress and deformation, measured directly by the extensometer, the stress-deformation curve is obtained (Figure 2.5).

Since in Figure 2.5 all the curves are very similar to one another, it is evident that all the specimens have a similar behaviour. As a consequence, all the tests are valid and repeatable and all the curves can be considered for the average values of the mechanical properties' calculation.

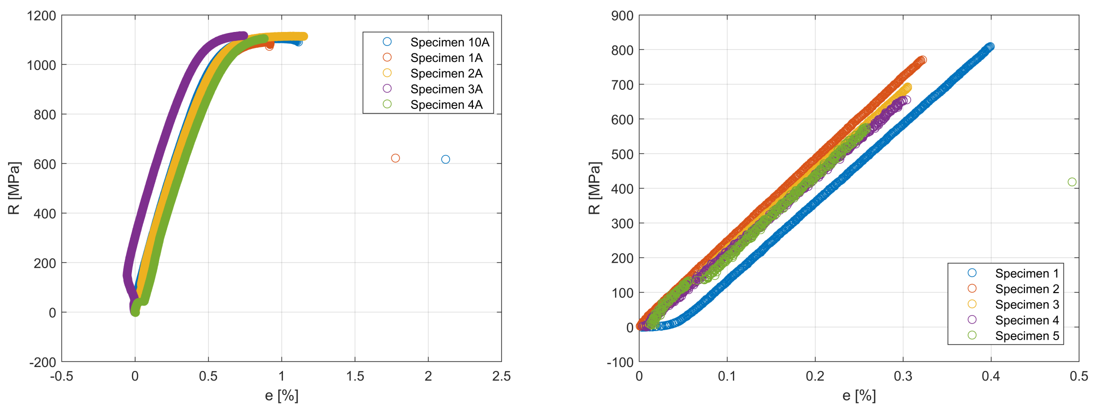

(a) *Non-treated specimen* **(b)** *Treated specimen*

Figure 2.5: *Stress - deformation curve*

Tensile strength

The tensile strength is the value of stress at the maximum force. It has been calculated for each specimen, then the results are organized as a normal distribution(Figure 2.6). This distribution has a level of confidence of the 95%.

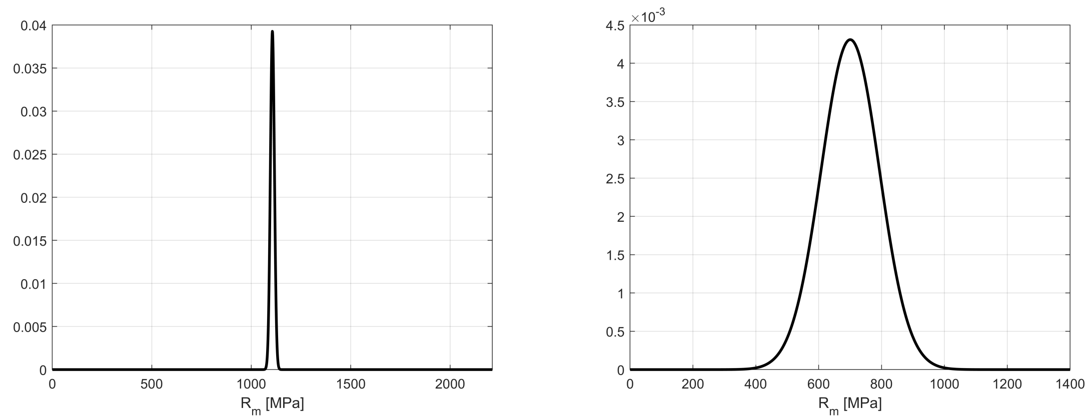

(a) *Non-treated specimen* **(b)** *Treated specimen*

Figure 2.6: *Tensile strength - normal distribution*

The mean values and the standard deviations are reported in Table 2.1.

Table 2.1: *Tensile strength normal distribution*

Material	Mean value	Deviation
Non-treated	1106,31 MPa	20,3 MPa
Treated	700,47 MPa	185,23 MPa

Yield strength

The yield strength can be determined only for the non treated specimen. This is due to the very brittle behaviour of the heat-treated specimens that do not exhibit a plastic behaviour.

Before the heat treatment, the CROVAC exhibits a continuous yielding. In particular, the yield strength correspond to the stress's value that produces a permanent deformation of the 0.2%. To find out this value, firstly the experimental data are interpolated with a straight line and then it has been shifted horizontally of 0.2%. The intersection between this line and the experimental data gives the yield strength. A graphical explanation of this procedure is reported in Figure 2.7.

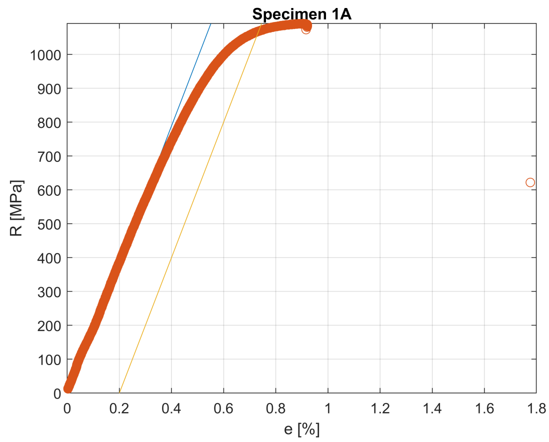

Figure 2.7: *Yield strength procedure*

The same procedure is followed for the other specimens and then a normal distribution with 95% level of confidence has been built (Figure 2.8).

The mean values and the standard deviations are reported in Table 2.2.

Table 2.2: *Yield strength normal distribution*

Material	Mean value	Deviation
Non-treated	1089,20 MPa	35,65 MPa

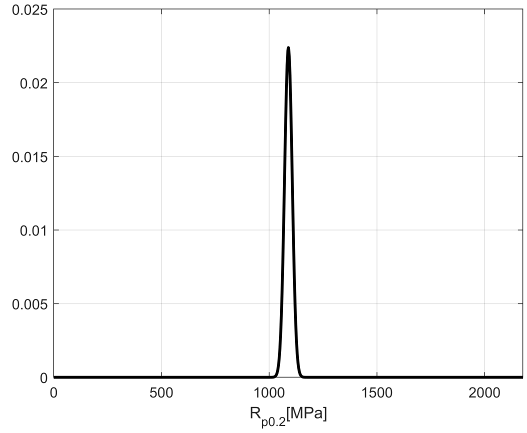

Figure 2.8: *Yield strength - normal distribution*

Total extension at maximum force

The total extension at maximum force is often used to measure the material's ductility. Also in this case, a normal distribution with a 95% level of confidence has been built (Figure 2.9):

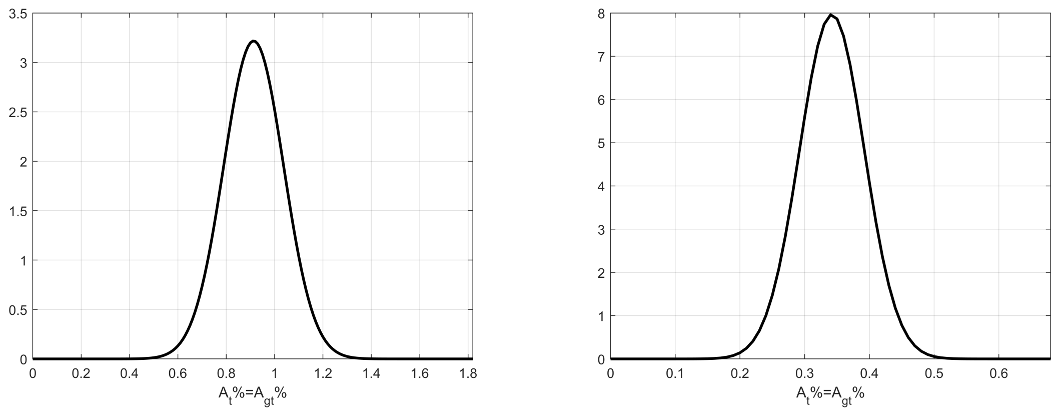

(a) *Non-treated specimen* **(b)** *Treated specimen*

Figure 2.9: *Total extension at maximum force - normal distribution*

The mean values and the standard deviations are reported in Table 2.3.

Table 2.3: *Total extension at maximum force - normal distribution*

Material	Mean value	Deviation
Non-treated	0,91%	0,24%
Treated	0,34%	0,1%

Elastic modulus

The elastic modulus has to be calculated following a prescribed procedure. Initially, in the stress-deformation curve a range of interest containing at leat 50 points has to be selected. Inside this range the experimental points are fitted using the least-squares method, obtaining an equation of the following type:

$$R = \frac{Ee}{100\%} + b \tag{2.3}$$

where:

1. R is the stress in MPa;
2. E is the modulus of elasticity in MPa;
3. e is the percentage extension;
4. b is the stress offset in MPa;

If the coefficient of correlation (R^2) is higher than 0.9995, the computation can be considered valid and E is the modulus of elasticity for the considered specimen. If this condition is not satisfied, the range has to changed until $R^2 > 0.9995$. In Figure 2.10 is reported this procedure for a specimen. In this case, $R^2 = 0.9998$ and the result is considered valid.

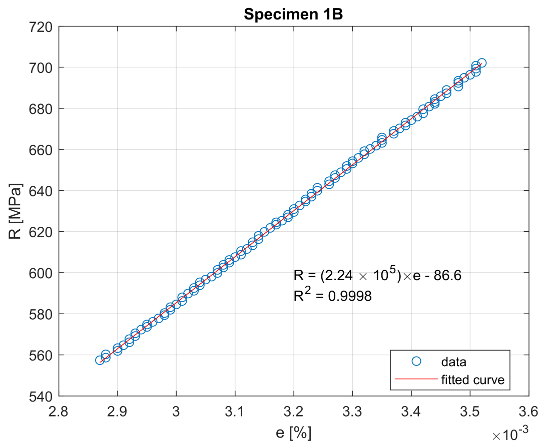

Figure 2.10: *Experimental data fitting*

Once the procedure is set up for all the specimens, the normal distribution for the modulus of elasticity can be calculated (Figure 2.11).

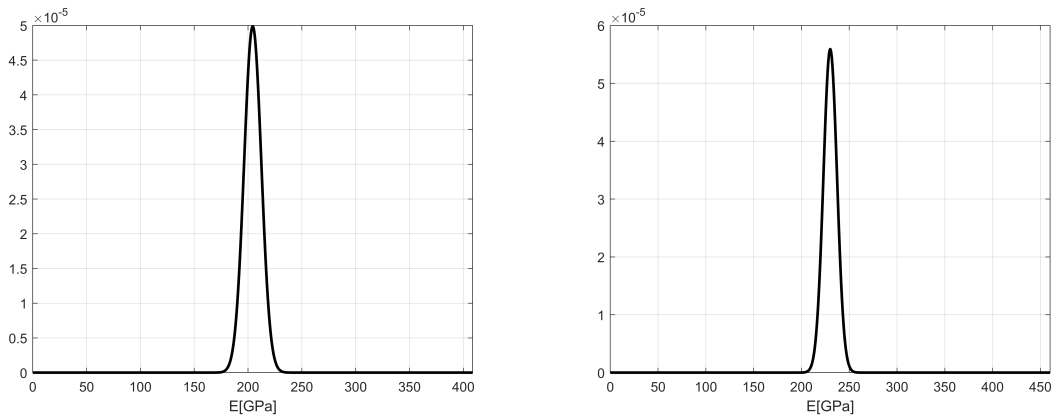

(a) *Non-treated specimen*

(b) *Treated specimen*

Figure 2.11: *Modulus of elasticity - normal distribution*

The mean values and the standard deviations are reported in Table 2.4.

Table 2.4: *Elastic modulus - normal distribution*

Material	Mean value	Deviation
Non-treated	204,29 GPa	15,99 GPa
Treated	230,11 GPa	14,27 GPa

2.1.3 Consideration on experimental results

In this paragraph the obtained results are commented. Firstly, the large deviation of the heat-treated specimen tensile strength demonstrates how the result is strictly related to the specimen manufacturing quality. Small defects due to the manufacturing process could easily trigger crack propagation because of the extreme brittleness of the material. Therefore, the measured tensile strength underestimates the real strength of the material. The tensile tests highlight also the brittleness of the CROVAC, that suddenly broke without any sign of yield. In fact, the heat-treated material's brittleness makes impossible the yield strength's calculation. Generally, the heat-treated CROVAC is more fragile and less ductile than the original material (the total extension is less for the treated specimen). Regarding the modulus of elasticity, the heat treatment makes the material stiffer.

The CROVAC shows better mechanical properties than the others SHMMs. However, it is supplied only in sheets, and for this reason the rotor cannot be made bulk but only laminated. This last consideration implies some disadvantages, especially from the mechanical point of view. In particular, the stiffness and the resistance of a laminated rotor are lower than the ones of a bulk rotor. Nevertheless, the rotor has been realized with CROVAC that offers a good mechanical resistance and good magnetic properties.

2.2 Rotor design

The rotor design is mandatory in order to reach the required rotational speed. Inner diameter and length of the rotor have already been chosen in order to satisfy the design requirements in terms of maximum torque, that has to be 0.3 Nm:

- $D_{in} = 8mm$;
- $L = 25mm$.

The stress analyses have led to the selection of the outer diameter.

2.2.1 Stress analysis

During its life, the rotor undergoes various load conditions. In the following analyses only the centrifugal load has been considered because the others load usually lead to negligible effects [20]. The analysis is carried out under the hypothesis of plain stress field that most of the time is verified for thin disks. In detail, this approach allows obtaining a closed-form solution. The plane stress field is characterized by only radial (σ_r) and tangential (σ_h) stresses, while shear stress disappear due to the problem axisymmetry. In the case of disk with a hole the stress field depends on the ratio between inner and outer radius ($\beta = \frac{r_i}{r_o}$) and on the radius r. The main relations are reported in equation 2.4. Analytical solutions of the problem can be found in [20], and they lead to the following formulation of σ_r and of σ_h

$$\begin{aligned}
&\sigma_r(r,\beta) = \rho\Omega^2 F_r(r,\beta) \quad , \\
&F_r(r,\beta) = \frac{3+\nu}{8} r_o^2 \left(1 + \beta^2\left(1 - \left(\frac{r_o}{r}\right)^2\right) - \left(\frac{r}{r_o}\right)^2\right) \\
\text{and}& \\
&\sigma_h(r,\beta) = \rho\Omega^2 F_h(r,\beta) \quad , \\
&F_h(r,\beta) = \frac{3+\nu}{8} r_o^2 \left(1 + \beta^2\left(1 + \left(\frac{r_o}{r}\right)^2\right) - \frac{1+3\nu}{3+\nu}\left(\frac{r}{r_o}\right)^2\right)
\end{aligned} \tag{2.4}$$

where Ω is the rotational speed, ν is the Poisson ratio of the material and ρ is te density of the material.

By considering the Von Mises criterion applied only to the principal plane stress case, the equivalent stress can be written as follows:

$$\begin{aligned}\sigma_{eq}(r,\beta) &= \sqrt{\sigma_r(r,\beta)^2 - \sigma_r(r,\beta)\sigma_h(r,\beta) + \sigma_h(r,\beta)^2} \\ \sigma_{eq}(r,\beta) &= \rho\Omega^2\sqrt{F_r(r,\beta)^2 - F_r(r,\beta)F_h(r,\beta) + F_h(r,\beta)^2} = \rho\Omega^2\bar{F}(r,\beta)\end{aligned} \tag{2.5}$$

It must be highlighted that these equations hold only for $\beta \in (0\,;\,1)$. From these equations it is clear that the rotor length doesn't influence the stress: this is due to the plain stress assumption. In literature [20], it is well known that the maximum equivalent stress is on the inner diameter, and for this reason it can be derived imposing $r = r_i$ in the previous equation.

The maximum spinning speed can be obtained from equation 2.5 by imposing the $\sigma_{eq}(r_i,\beta)$ equal to the CROVAC tensile strength.

$$\Omega_{Max} = \sqrt{\frac{S_{UT}}{\rho\bar{F}(r_i,\beta)}} \tag{2.6}$$

On the material strength, a safety factor of 1.4 has been considered. Due to the non-linearity of the equation to determine the outer diameter is convenient to calculate the maximum spinning speed imposing different value of r_o and therefore of β. In Figure 2.12 the results are reported: it must be pointed out that, under the same inner diameter, higher spinning speed can be achieved through lower outer diameter.

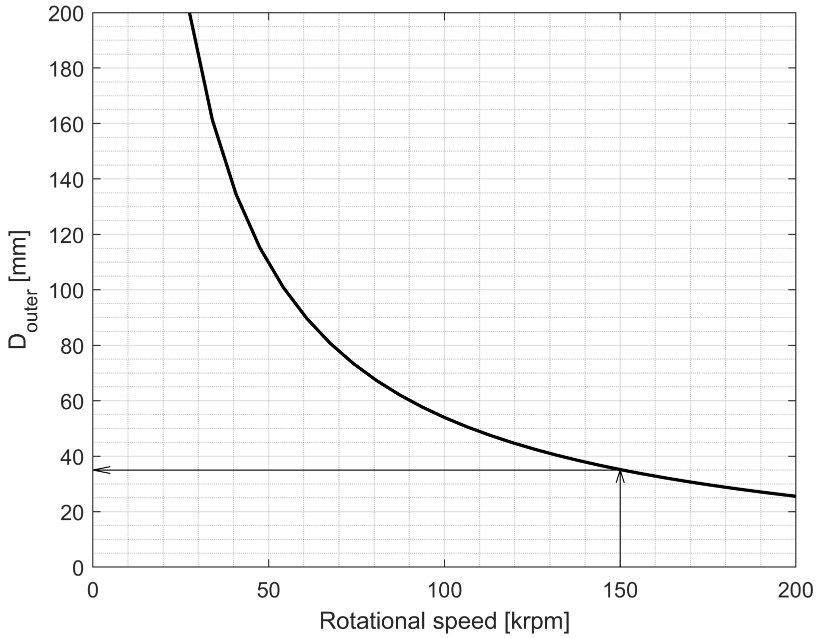

Figure 2.12: *Maximum achievable rotational speed vs outer diameter*

In that case, to reach the required spinning speed of 150 krpm the outer diameter has to be set equal to 35 mm.

To verify the correctness of the analytical results, a 2D FEM stress analysis with COMSOL has been performed. The obtained results are reported in Figure 2.13.

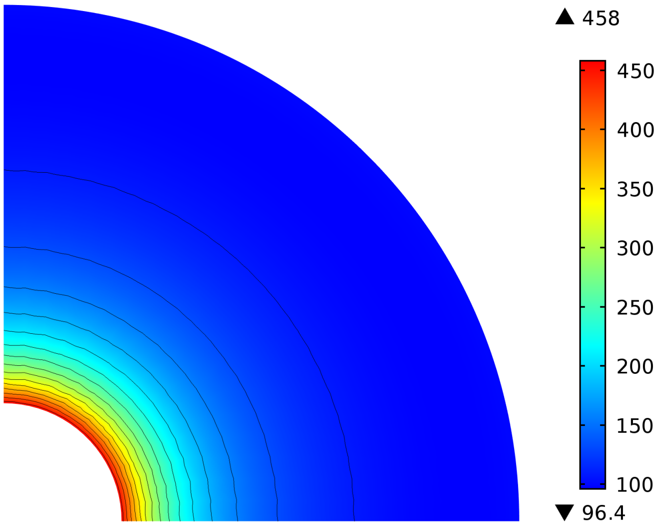

Figure 2.13: *Stress field on the rotor*

In particular, the analysis performed in COMSOL confirms the analytical results previously obtained and highlights that the maximum stress reached in the disk is of 441 MPa at the inner diameter. Considering this value of stress the rotor can spin at 150 krpm with a safety factor on the yield strength equal to 1.5.

2.3 Rotor manufacturing

This section describes how the rotor has been manufactured. The CROVAC is supplied by VACUUMSCHMELZE as sheets with a thickness of 0.25 mm. Starting from these sheets a photoengraving process is performed to obtain circular sheets with an inner diameter of 8 mm and an outer diameter of 35 mm (Figure 2.14). By design, the rotor

Figure 2.14: *CROVAC sheets*

length is set at 25 mm, and, consequently, it is necessary to join about 100 sheets. In particular, to join all the sheets together, it is decided to use the glue based on epoxy resin UHU PLUS ENDFEST 300. This glue is a two-component type: it is composed by a binder and a hardener which must be mixed in varying proportions. In this case, a 1:1 volume mix between the two components is chosen. This mix allows to have a good compromise between the hardness of the end product and the resistance to heat, water and chemical substances. Before applying the glue, each sheet is accurately washed with a diluent in order to remove every type of impurity on the surface. Then the glue is applied to each sheet and finally all the sheets are pressed between two steel elements in order to eliminate the glue in excess. The mechanism used to push the sheets is reported in Figure 2.15, it consists of 2 steel discs with a calibrated screw that allows the tightening of the plates inside. The calibrated screw is adjusted in such a way as to meet the tolerances imposed by the internal diameter of the plates. Once the central screw is tightened, three screws are placed laterally and the central screw is removed. In this way, the central screw of the rotor is not glued to the rotor.

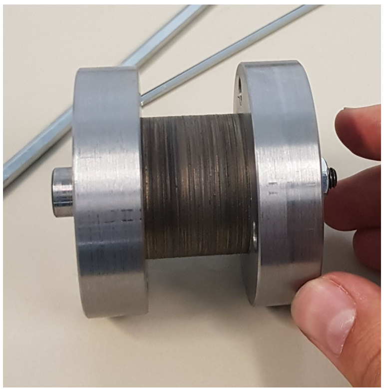

Figure 2.15: *Mechanism to push the CROVAC sheets*

At this point, the hardening process is carried out. It can take place at different temperature and the final resistance will be function of them. In order to have a strong adhesion, the glued sheets are placed in an oven at 150 °C for 5 minutes and then cooled down at room temperature. Subsequently, the rotor is machined on the lathe both at the inner and on the outer diameter, in order to remove irregularity on the geometry and to respect the imposed tolerance, and therefore to allow an easier coupling with the shaft. Finally, the rotor is connected to the shaft and grinded in order to be centred with respect to the bearings.

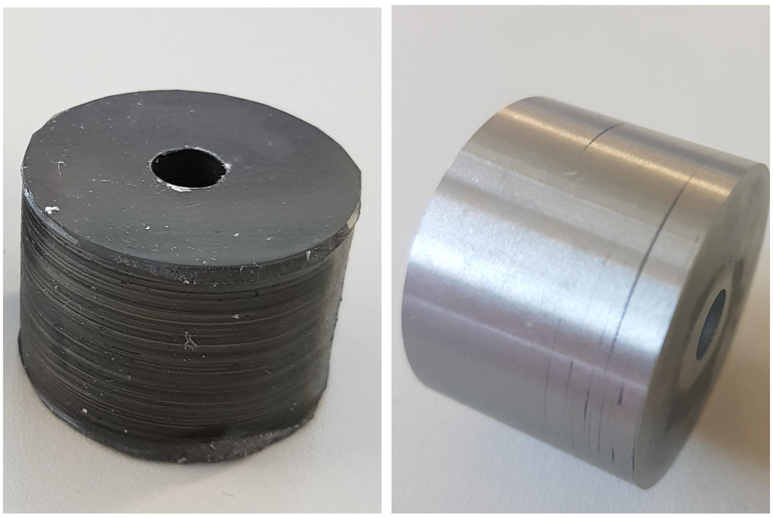

(a) *Before machining* **(b)** *After machining*

Figure 2.16: *Final CROVAC rotor*

The rotor mounted on the shaft is reported in figure 2.17.

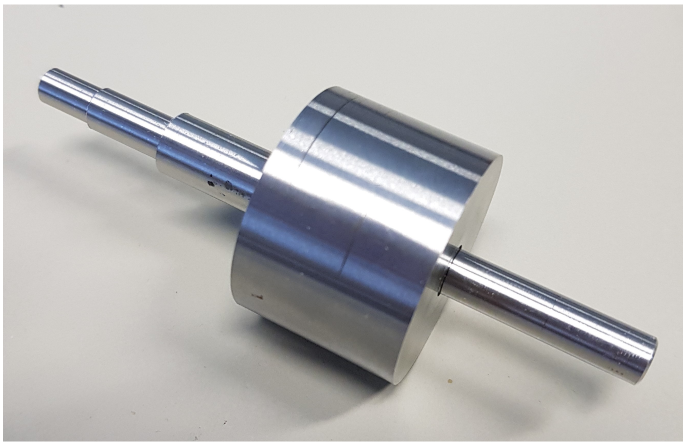

Figure 2.17: *Final rotor*

2.4 Prototype layout

Once the rotor has been designed, it has been inserted into the stator previously designed to test the operation. The layout proposed for the hysteresis machine is the one shown in Figure 2.18. The machine can be considered as a cylindrical-inner rotor machine composed of a conventional stator (6) with 12 slots and distributed windings made of rolled steel NO20 (sheet thickness 0.2 mm). The rotating part is made by a 316l stainless steel shaft (4), while the active part (1) is made of CROVAC 12/160 laminated hysteresis material (sheet thickness 0.25 mm). The shaft is characterized by a low inertia: this allows rapid transient phase, a very important peculiarity for turbo-compound. The shaft is supported by 2 X-mount bearings (SKF 707ACDHCP4AH), each fixed to the cover by two O-Rings made of NBR with a shore hardness of 70 (2). The bearings are pre-loaded with a spring (3). This type of bearing allows to reach high speed, minimizing the friction losses. In addiction, the O-Rings have a dual function: the first is to seal the bearings and prevent oil leakage, on the other hand they also have a damping function that allows to reduce the amplitude of the oscillations. The bearings have an oil-air lubrication through a special hydraulic unit. The whole motor is contained inside an aluminium 1060 case (5).

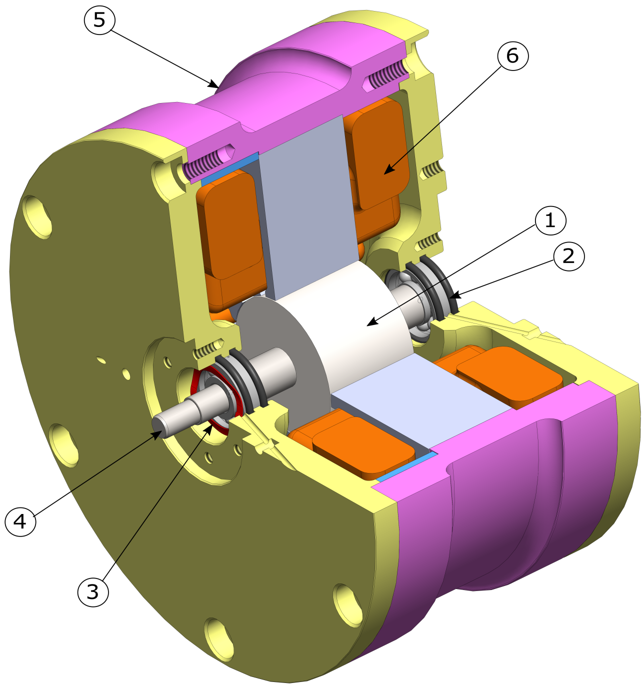

Figure 2.18: *Hysteresis machine*

The main characteristics of the hysteresis machine are resumed in Table 2.5:

Table 2.5: *Hysteresis machine characteristics*

Maximum speed	150 krpm
Maximum torque	0.3 Nm
Stator outside diameter	115 Nm
Rotor inside diameter	8 mm
Rotor outside diameter	35 mm

Chapter 3

Free-free rotor: modelling and validation

In this chapter the dynamic of the rotor in free-free condition has been studied. Initially, three different finite element models have been proposed with the aim of identifying the contribution of the rotor in terms of stiffness. Then, experimental tests were carried out in order to choose the most suitable FEM model. This step allowed to validate the model related to the rotordynamics. Subsequently, spacers and bearings have been added to the model and it has been also validated. These experimental tests have allowed to validate the finite element model independently of the supports' dynamic, which will be discussed in the next chapter.

3.1 Overview on rotordynamic

Rotordynamic is a specialized branch of the applied mechanics dealing with the study of mechanical devices in which one or more parts, called rotors, are constrained with a set of bearing or hinges to rotate about a fixed axis. The rotor that belongs to this category are known as *constrained rotor*. However, there are cases in which there isn't any constraint to the rotor: in this case the rotor is referred as *free rotor*. Rotating machinery can experience two type of motion while they're working: they spin about their axis and whirl about the deformed axis line (*precession*). The studies on rotor are mainly focused on the *precession* motion, and it can be compared to the vibration of the static structure. During this motion, there are speeds across which the vibrations reach the maximum, and they are called *critical speeds*. The vibrations are mainly due to the fact that these machines are unbalanced. In particular, two types of unbalance are defined: *static unbalance* is the condition for which the center of mass doesn't coincide with the geometric centre and, it is mainly due to manufacturing errors; *dynamic unbalance* is the condition for which the principal axis of inertia doesn't coincide with the spinning axis of the machine and, it is mainly due to mounting errors. Usually these two types of unbalance come together and the expression *couple unbalance* is used.

If the amplitude of the vibrations is too high, failure can occur. For this it is important an accurate study of the dynamic of the rotor.

The simplest model to study the rotordynamics is the Jeffcott rotor: it consists in describing the rotor as a point mass neglecting its moment of inertia. This model is able to describe different physical phenomena like self-centering in super-critical regime and the roles of the damping, but it cannot describe others important phenomena like the dependence of the natural frequency with the spinning speed. To take in account the latter phenomena the 4-DOF rigid rotor model can be used: the rotor is considered both in terms of mass and of moment of inertia. The moment of inertia has an important role in the flexural behaviour of the rotor, in fact it is responsible for the gyroscopic effect, that causes a variation of the natural frequencies with the spinning speed. However, these models don't give accurate description of the rotor's behaviour. If an accurate analysis is requested the flexible rotor can be modelled, theoretically, as a continuum model. However, the resulting equations are partial derivative differential equation that can be solved in a closed form only in few particular cases. For this, numerical techniques are often used. In the rotordynamic field, two techniques are particularly spread: the *lumped-parameters methods* and the *finite element method* (FEM). Among the *lumped-parameters methods*, the most famous is the *Myklestadt-Prohl method*.

In this work, the *finite element method* (FEM) has been used.

3.2 Rotor modeling

The rotor has been modelled with DYNROT. It is a finite element code, written in Matlab by Genta et Al. [21], that allows the calculation of the main rotordynamic features. In particular, the rotor is modelled as Timoshenko beam-like elements. Each element is composed of two nodes, and each node has 6 degree of freedom (DOF). In Figure 3.1 the different DOFs of each node are reported: u_x, u_y, u_z are the displacement along x,y,z axis, respectively, while ϕ_x, ϕ_y, ϕ_z are the rotations about each axis. Thus, the software allows to study the axial, torsional and flexural behaviour of a rotor. Besides the beam element, the code contains many elements such as mass, spring,

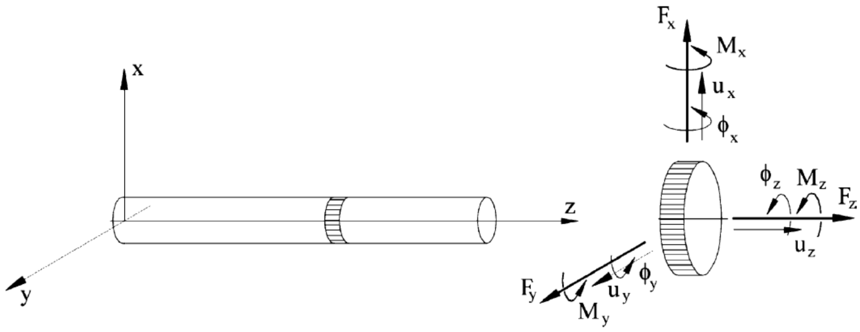

Figure 3.1: *DOF and force on a generic cross-section*

damper, magnetic bearings, which allow to have a proper modelling of any component.

If the axis of the beam is assumed to be straight and if the cross-section has two perpendicular planes of symmetry the flexural behaviour is uncoupled from the axial and torsional ones. To define the flexural behaviour of a beam for each node 4 DOFs are necessary: u_x and u_y describe the translation on x and y direction while ϕ_x and ϕ_y describe the rotation about x and y axes. In DYNROT complex DOFs are considered, this allows to halve the dimensions of the problem:

$$\begin{cases} u_z = u_x + j u_y \\ \phi = \phi_y - j\phi_x \end{cases} \tag{3.1}$$

where j is the imaginary unit. The software allows to find all the matrices of interest in describing the dynamic behaviour of the rotor.

The general equation for a rotor that is rotating with an angular speed Ω is well-known in literature [22], and it is reported in equation 3.2 for the sake of completeness.

$$[M]\{\ddot{q}\}+([C_n]+[C_r]-j\Omega[G])\{\dot{q}\}+([K]+\Omega^2[K_\Omega]\pm j[K_n^{''}]\pm j[K_r^{''}]-j\Omega[C_r])\{q\} = \Omega^2\{f\}e^{j\Omega t} \tag{3.2}$$

where [M] is the mass matrix, [K] is the stiffness matrix, [G] is the gyroscopic matrix, $[C_n]$ and $[C_r]$ are the matrices of non-rotating and rotating viscous damping, $[K_n^{''}]$ and $[K_r^{''}]$ are the matrices of the non-rotating and rotating hysteretic damping. The term $\Omega^2[K_\Omega]$ takes the centrifugal stiffening into account. $\{q\}$ is the vector of complex coordinates and f is the vector of unbalance forces at each node:

$$f = \begin{Bmatrix} m\epsilon e^{j\alpha} \\ \chi(J_t - J_p) \end{Bmatrix} \tag{3.3}$$

where J_t and J_p are respectively the transversal and polar moment of inertia.

Equation 3.2 can be written in the state-space:

$$\{\dot{z}\} = [A]\{z\} + [B]\{u\}. \tag{3.4}$$

The state vector z is defined as:

$$z = \begin{Bmatrix} \dot{q} \\ q \end{Bmatrix} \quad . \tag{3.5}$$

The corresponding state matrix A and input $[B]\{u\}$ are:

$$[A] = \begin{bmatrix} -M^{-1}([C_n] + [C_r] - j\Omega[G]) & -M^{-1}([K] + \Omega^2[K_\Omega] \pm j[K_n''] \pm j[K_r''] - j\Omega[C_r]) \\ I & 0 \end{bmatrix}, \tag{3.6}$$

$$[B]\{u\} = \Omega^2 \begin{bmatrix} M^{-1}\{f\} \\ 0 \end{bmatrix} e^{j\Omega t}. \tag{3.7}$$

The eigenvalues of the dynamic matrix A are the natural frequencies: usually they are function of the angular speed. The eigenvectors of the dynamic matrix are the mode shapes. If the unbalance response has to be determined, the second set of the state space equation is introduced:

$$\{y\} = [C]\{z\} + [D]\{u\}. \tag{3.8}$$

In particular if the displacement of the centre of gravity's node g has to be found, the matrices C and D of equation 3.8 become:

$$[C] = [A(2g-1,:)], \tag{3.9}$$

$$[D] = [0]. \tag{3.10}$$

In case of a free-free rotor the dynamic matrix A and the input $[B]\{u\}$ become:

$$[A] = \begin{bmatrix} -M^{-1}([C_n] + [C_r]) & -M^{-1}([K] \pm j[K_n''] \pm j[K_r'']) \\ I & 0 \end{bmatrix}, \tag{3.11}$$

$$[B]\{u\} = \begin{bmatrix} M^{-1}\{f_{input}\} \\ 0 \end{bmatrix} \tag{3.12}$$

where $\{f_{input}\}$ is a generic input to the rotor. The eigenvalues of the dynamic matrix A are the natural frequencies of the free-free system, while the eigenvectors are the mode shapes.

In particular if the acceleration due to a single input of the node k has to be found, the matrices C and D of the equation 3.8 become:

$$[C] = [A(k,:)], \tag{3.13}$$

$$[D] = [B(k,:)]. \tag{3.14}$$

3.3 Numerical results

The free-free rotor model is useful to identify the mass and stiffness properties of the rotor, without considering the supports' dynamic.

The CAD model of the rotor is reported in Figure 3.2. The bearing on the left side

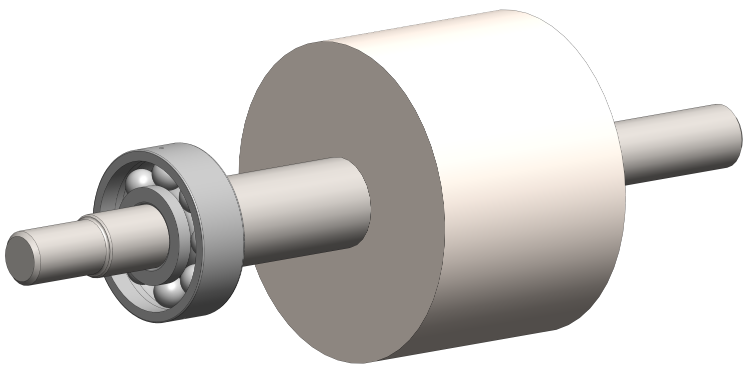

Figure 3.2: *CAD model of the rotor*

cannot be removed for the test because it is mounted with shrink fit and some damage can occur in the disassembly process. The shaft has been realized with stainless steel 316L while the rotor is made with CROVAC. The main properties of the two materials are reported in the tables 3.1 and 3.2.

Table 3.1: *Stainless steel 316L characteristics*

E	200 GPa
ρ	7900 kg/m^3
η	10^{-3}
ν	0.28

Table 3.2: *CROVAC characteristics*

E	230 GPa
ρ	7700 kg/m^3
η	10^{-3}
ν	0.28

The main goal of this part is to identify how the rotor contributes to the shaft's stiffness. To accomplish to this task, this three different models have been analysed: in the first one the rotor is considered as non-structural, so it gives contribution only in terms of inertia; in the second one the rotor is considered as structural, so it gives a full contribution in terms of stiffness; in the last one the rotor is modelled as semi-structural, so it increased of a certain quantity the shaft's stiffness.

3.3.1 Non-structural rotor

The FEM model, considering the non-structural rotor, is reported in figure 3.3. The shaft has been modelled with 102 beam elements, and for all the models this mesh will be used. In this way effects related to the variation of discretization are excluded.

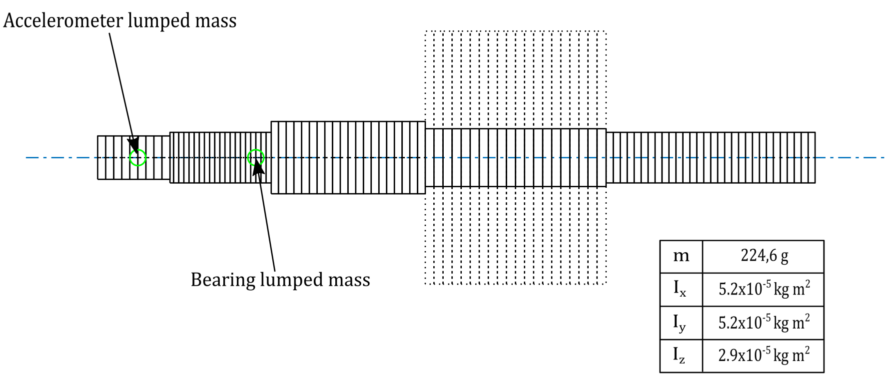

Figure 3.3: *Non-structural rotor mesh*

The bearing is modelled as a concentrated mass of 7 g and, for reasons depending on the experimental acquisitions, it is also necessary to add the mass of the accelerometer (1.4 g). The natural frequencies of the rotor are reported in the table 3.3.

The mode shapes are reported in figure 3.4. The red dotted-line indicates the not-deformed configuration while the black dotted-line refers to the deformed one.

Being the rotor free, other two modes at 0 Hz have been found, however they represent the rigid body motion of the system and they are not of interest.

Table 3.3: *Natural frequencies*

ω_1	2573 Hz
ω_2	5100 Hz

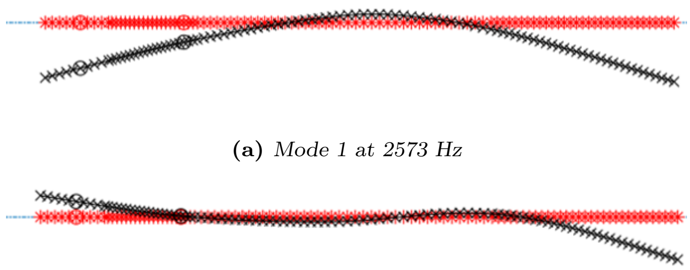

(a) *Mode 1 at 2573 Hz*

(b) *Mode 2 at 5100 Hz*

Figure 3.4: *Modal shapes*

3.3.2 Structural rotor

In this part the rotor has been considered as structural: so it is rigidly connected to the shaft. The FEM model is reported in figure 3.5. Also in this case two concentrated mass

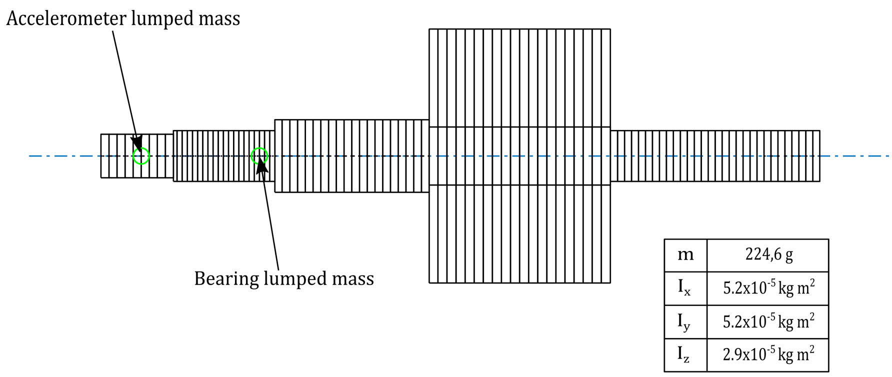

Figure 3.5: *Structural rotor mesh*

for both the bearings and the accelerometer have been put. The natural frequencies are reported in table 3.4.

The mode shapes are calculated, and they are reported in figure 3.6.

Table 3.4: *Natural frequencies*

ω_1	4623 Hz
ω_2	6398 Hz

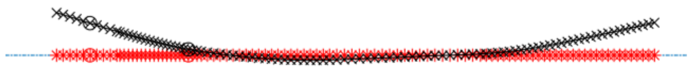

(a) *Mode 1 at 4623 Hz*

(b) *Mode 2 at 6398 Hz*

Figure 3.6: *Modal shapes*

3.3.3 Semi-structural rotor

In this section the rotor is modelled as semi-structural mass: it gives a partial stiffness contribution to shaft. This partial contribution has been modelled by modifying the Young modulus of the shaft in correspondence of the rotor and the rotor itself has been modelled as a distributed mass. This procedure is widely used in literature, as shown in [23]. The FEM model of the shaft is reported in figure 3.7. In this case the Young

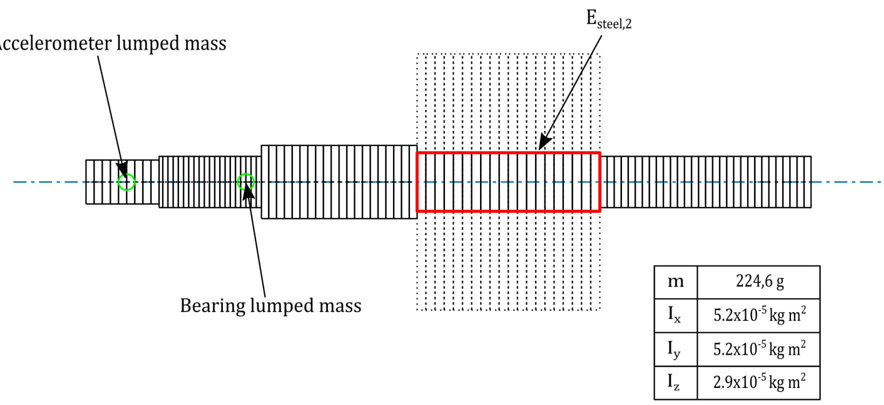

Figure 3.7: *Structural rotor mesh*

modulus of the shaft in correspondence of the rotor has been increased to 350 GPa.

The natural frequencies of the system are reported in the table 3.5.

The mode shapes are calculated, and they are reported in figure 3.8.

Table 3.5: *Natural frequencies*

ω_1	2947 Hz
ω_2	5159 Hz

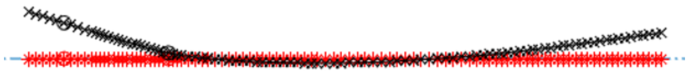

(a) *Mode 1 at 2947 Hz*

(b) *Mode 2 at 5159 Hz*

Figure 3.8: *Modal shapes*

3.4 Experimental tests

The hammering experimental tests have been conducted on the free-free rotor to validate the FEM model. The rotor has been hammered in two different points while the accelerometer remains always in the same position. From this test two different FRFs have been found, and they allow to identify the first two natural frequencies. In that way it has been found the best model among the three previously analysed, then, the match between the FRFs of the chosen model and the experimental one have been analysed.

3.4.1 FRF determination

Nowadays, the hammering test is one of the most used technique in order to find the frequency response function (FRF) of a structure. It consists in exciting a structure with an hammer provided of a load cell that is able to measure the produced force. This force is equal and opposite with respect to the one acting on the structure. On the structure is also positioned an accelerometer in order to measure the acceleration of the structure in a point. The signal of the hammer force and the one of the accelerometer are elaborated by a software that reconstructs the FRF. A scheme of this procedure is reported in figure 3.9.

The quality of the measurements depends mainly on the energy transferred to the structure that must be sufficiently large to excite the desired modes. This energy is proportional to the excitation force that depends mainly on two parameters: tip mass

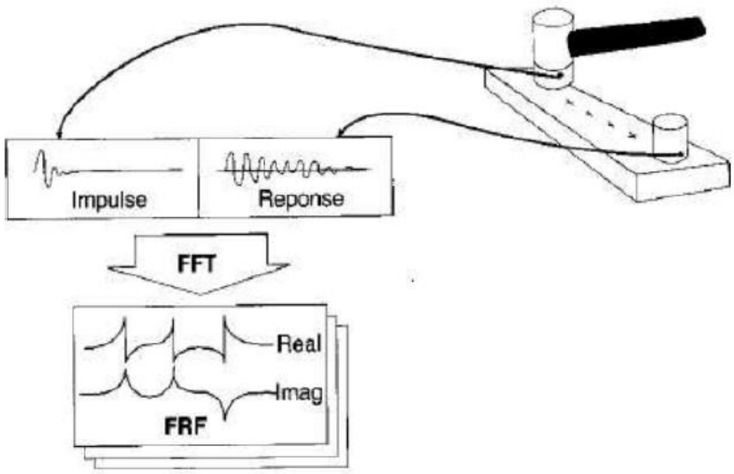

Figure 3.9: *FRF experimental acquisition with hammering*

of the hammer and speed of impact. To explain the influence lets consider the force as rectangular impulse with unit amplitude and duration 2a (Figure 3.10).

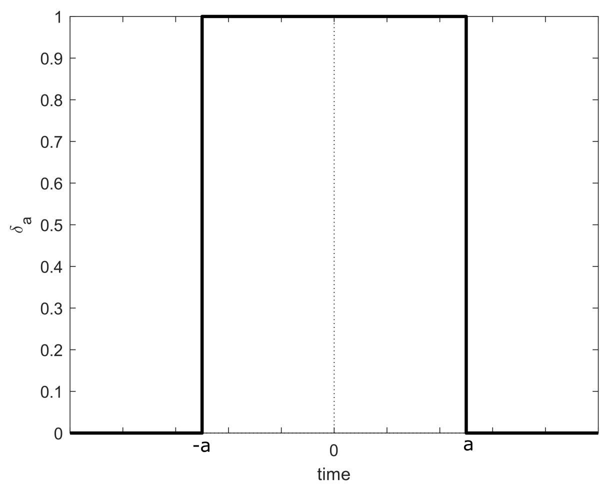

Figure 3.10: *Rectangular impulse*

The Fourier transform of this signal is:

$$F[\delta_a(t)] = \int_{-a}^{a} e^{-i\omega t}\, dt = 2a \times \frac{\sin(a\omega)}{a\omega} \tag{3.15}$$

In figure 3.11 is reported the Fourier transform of the rectangular impulse.

The amplitude of the signal is inversely proportional to the maximum excited frequency. To control the excited frequency band, the stiffness of the tip of the hammer

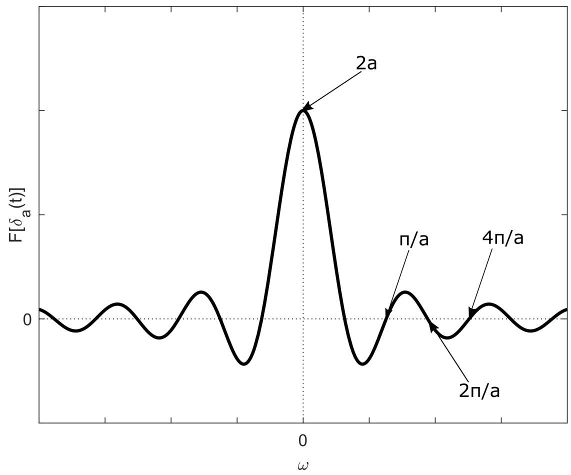

Figure 3.11: *Fourier trasform of the rectangular impulse*

must be acted upon, as a stiffer tip generates a pulse much more similar to an ideal impulse and therefore with a very short duration. So the stiffer the tip of the hammer, the greater the excited frequency band, and lower is the energy transferred to the system. Therefore, it is needed a trade-off between the energy transferred to the structure and the maximum excited frequency. This can also be seen from the figure 3.12.

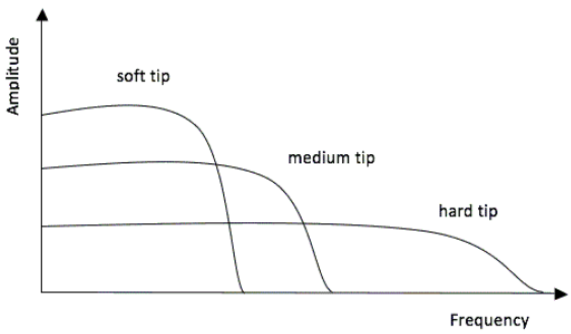

Figure 3.12: *Frequency band as function of tip hardness*

Usually, different measurements are done on the same points and then an average FRF is build by the software. To assess if all the measurements are correct, the coherence function can be used. It is a function proportional to the ratio between signal and noise that can assume value between 0 and 1. If this function goes below 0.75 the measurement must be discarded and the test has to be repeated.

To ensure the accuracy of the test, the direction of the applied force has to be considered: it must be as parallel as possible to the axis of the accelerometer.

3.4.2 Experimental setup

The components needed to do the tests are reported in figure 3.13. The shaft is

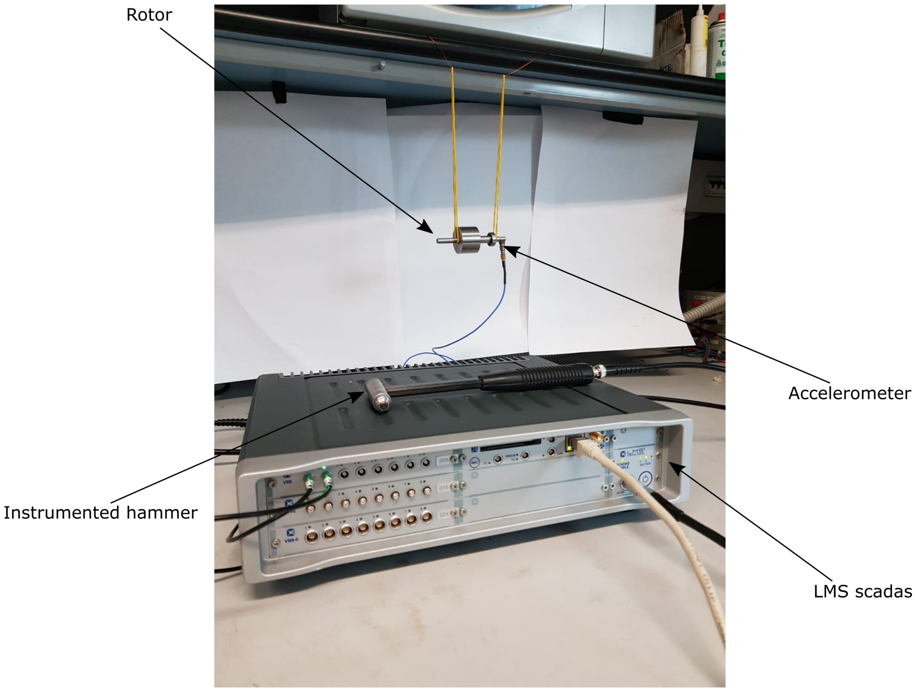

Figure 3.13: *Experimental setup*

hung with elastics to avoid a contribution in terms of stiffness that would produce a variation of natural frequencies. The oscillations due to the elastic take place at low frequency and therefore do not interfere with the measurements. A mono-axial accelerometer PCB Piezotronics has been used, the maximum frequency it can analyse is 10 kHz. The accelerometer has been fixed with a wax to the shaft. The instrumented hammer is used with the stiffer tip available, in this way all the frequencies of interest have been excited. The accelerometer and the hammer have been connected to the acquisition system SCADAS, connected to the PC with an ethernet cable. The data are processing on the PC through the software LMS Test.Lab (Siemens). Before doing the acquisition, it is necessary to set the sensitivity of the instrument on the software. Once the acquisitions were carried out, the files have been exported in MATLAB.

3.4.3 Experimental results

The experimental tests allow to find two different FRFs. The first is reported in figure 3.14 and it refers to the collocated case:the shaft has been hammered in correspondence to the accelerometer. The second FRF was obtained by hammering the shaft at the opposite end to where the accelerometer was positioned: the results of this test are shown in the figure 3.15.

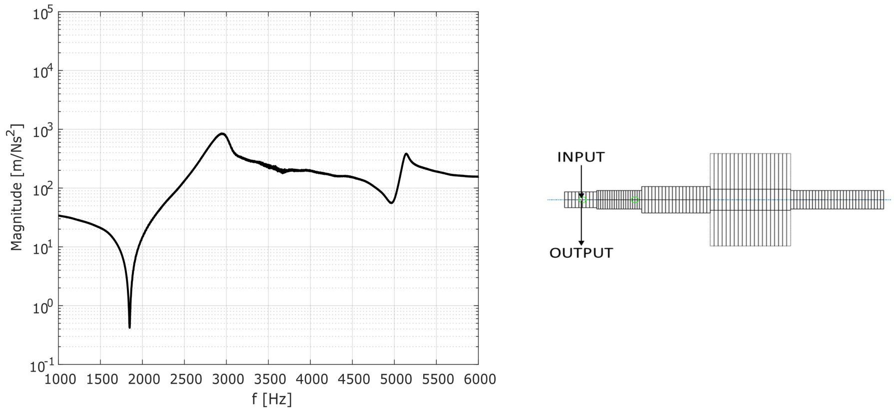

Figure 3.14: *Experimental FRF - Collocated*

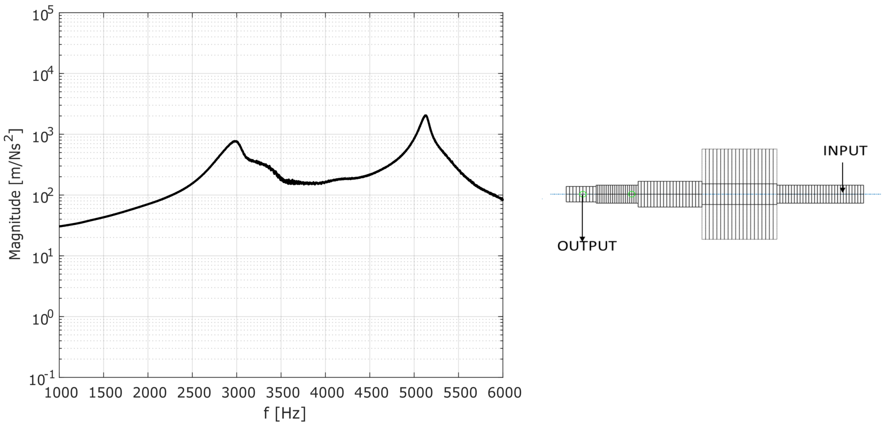

Figure 3.15: *Experimental FRF - Non-collocated*

These results show that the peaks of the two transfer functions are at the same frequencies. Consequently, the reliability of the test is demonstrated and the first two natural frequencies are identified. The values of the natural frequencies are shown in the table 3.6.

Table 3.6: *Experimental natural frequencies*

ω_1	2957 Hz
ω_2	5151 Hz

3.4.4 Model validation

Once the experimental natural frequencies are known, a comparison has been made between the experimental natural frequencies and the ones provided by the various numerical models. To carry out this comparison, the error between the experimental and numerical frequencies was calculated using the equation 3.16.

$$\epsilon = \frac{\omega_{exp} - \omega_{model}}{\omega_{exp}} \times 100 \tag{3.16}$$

Then the results are reported in the histogram of figure 3.16.

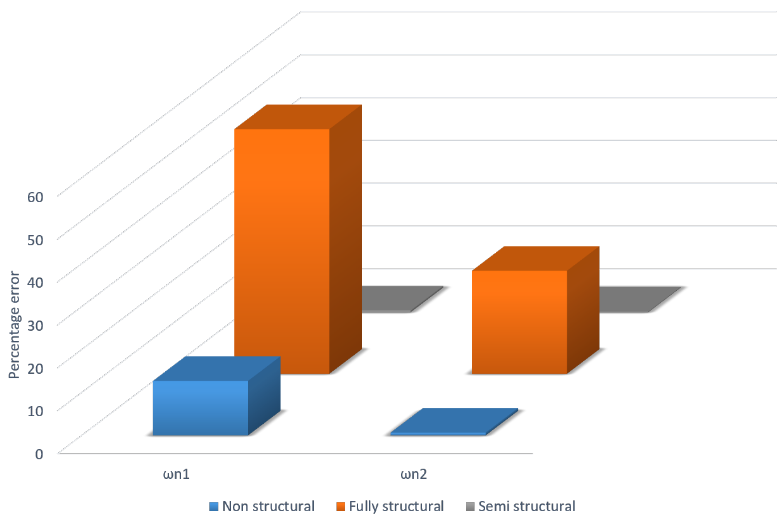

Figure 3.16: *Percentage error of the different models*

The model, that most closely describes the experimental natural frequencies, is the one with the semi-structural rotor described in paragraph 3.3.3.

Then, the transfer functions determined with this model are compared to the transfer functions determined experimentally. The numerical transfer functions have been calculated with the equations 3.8, 3.13 and 3.14. In figure 3.17 is reported the experimental and numerical FRF for the collocated case, while in figure 3.18 is reported the FRF for the non-collocated case.

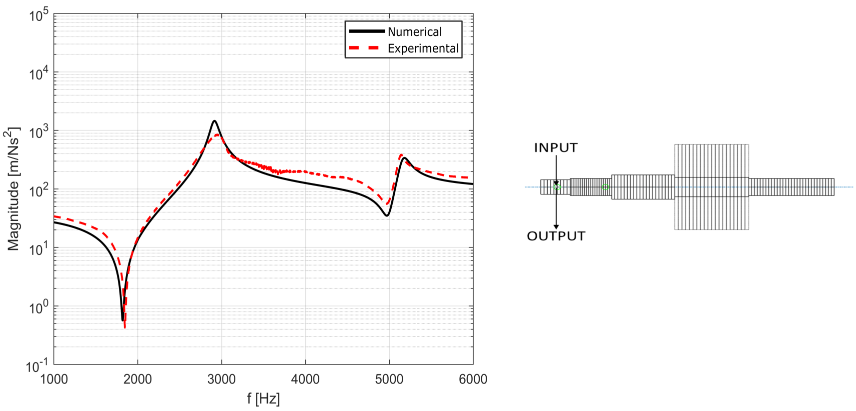

Figure 3.17: *Colocated FRF*

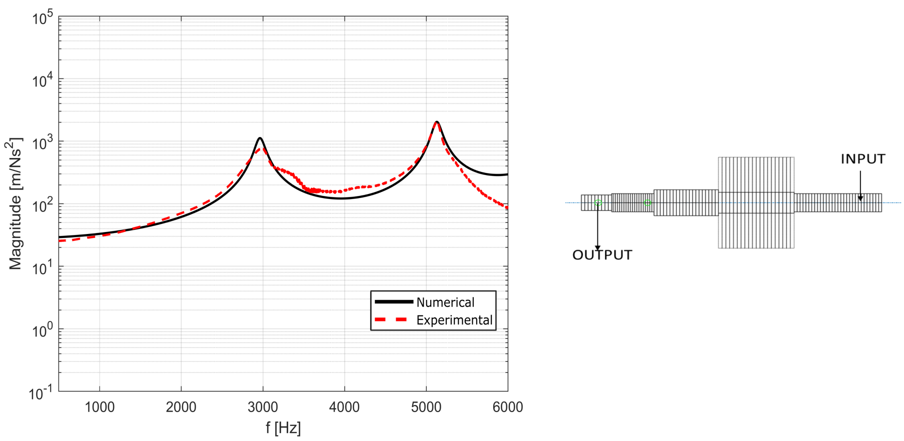

Figure 3.18: *Non-colocated FRF*

The semi-structural rotor model predicts appropriately the behaviour of the real rotor at least up to 6000 Hz, so it can be considered valid for the description of rotor behaviour. Finally, other components, like bearing and spacer, are added to the model and a further analysis is performed to study the overall behaviour.

3.5 Model with spacer and bearings

While in the previous section the dynamic model of the shaft has been validated considering only one bearing, in this section the aluminium spacer and the other bearing have been added and the overall behaviour has been studied. This allows to completely characterize the dynamics of the shaft at standstill without considering the effect of the supports. The CAD model of this component is shown in the figure 3.19.

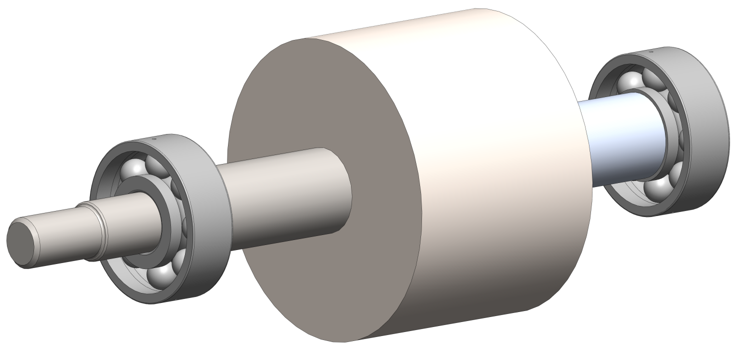

Figure 3.19: *CAD model*

Also in this case the FEM model was built on DYNROT, the bearings were considered as concentrated mass while the spacer as non-structural mass. For this reason, it is only necessary to define the density of the aluminium, which has been set at $2700 kg/m^3$. In this case, the spacer can be modelled as non-structural mass since it is mounted with play and therefore cannot make a contribution in terms of stiffness. The FEM model is reported in figure 3.20.

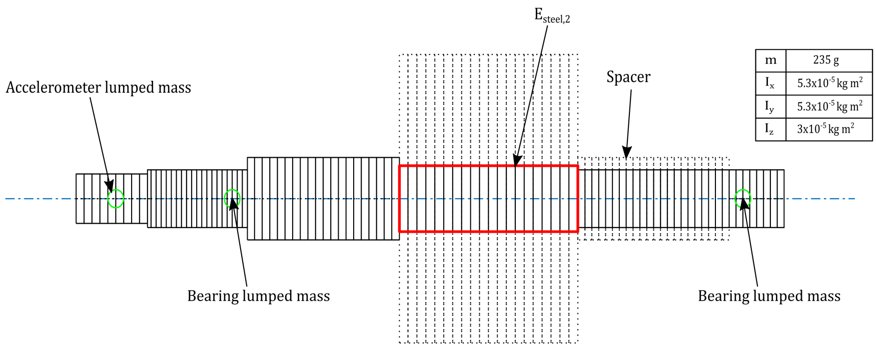

Figure 3.20: *FEM model with spacer*

The natural frequencies obtained from the numerical model are shown in table 3.7:

Table 3.7: *Natural frequencies*

ω_1	2800 Hz
ω_2	4350 Hz

The natural frequencies of this model are lower than the ones identified in the previous model. This is due to the added mass (spacer) that does not give any contribution in terms of stiffness. Then, the modal shapes have been calculated and, they are reported in figure 3.21.

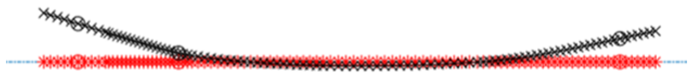

(a) *Mode 1 at 2800 Hz*

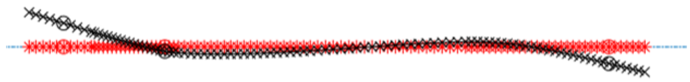

(b) *Mode 2 at 4350 Hz*

Figure 3.21: *Modal shapes*

3.5.1 Experimental validation

The same steps were followed for the experimental validation process as explained in section 3.4. In this case only the co-located test could be performed for lack of space, as it would not make sense to excite the structure hammering the spacer.

The transfer function obtained experimentally and the numerical function were superimposed in the figure 3.22.

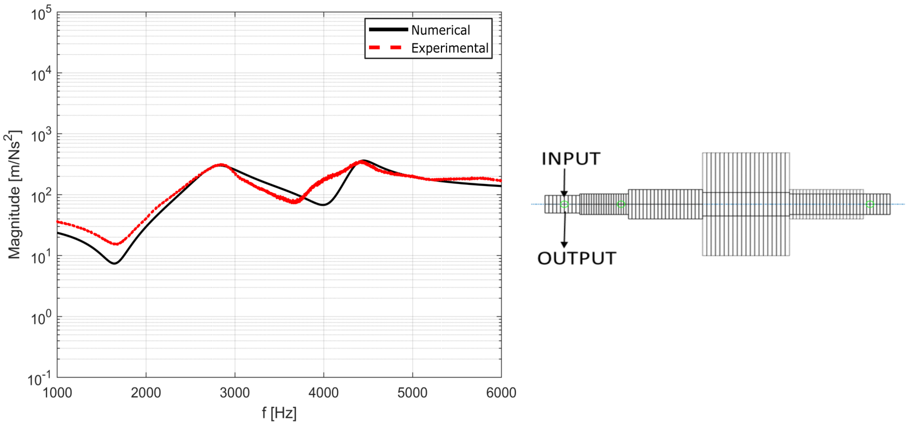

Figure 3.22: *Colocated FRF*

Also in this case the natural frequencies obtained numerically are close to the natural frequencies obtained experimentally. In addition, the experimental FRF is comparable with the numerical FRF. For this reason, also this model can be considered validated and this allows passing to the analysis of the dynamics of the supports.

3.6 Sensitivity analysis on axial dynamic

When the elasticity modulus is modified only in a particular region of the shaft, the model still behaves successful if the flexural dynamic is considered. Indeed, if the axial dynamic is considered a modification of the elasticity modulus implies surely a variation of the axial natural frequencies of the numerical model, that could not correspond to a variation of the axial natural frequency of the real system. This aspect is due to different contribution the rotor could have in terms of stiffness when the axial and flexural dynamics are considered. In this section, the influence of that modification on the axial dynamic is studied and analysed.

Initially, the first two axial natural frequencies have been studied for both the model with the non-structural rotor of section 3.3.1 and the model with the semi-structural rotor of section 3.3.3. The results are reported in figure 3.23. The picture 3.23 shows

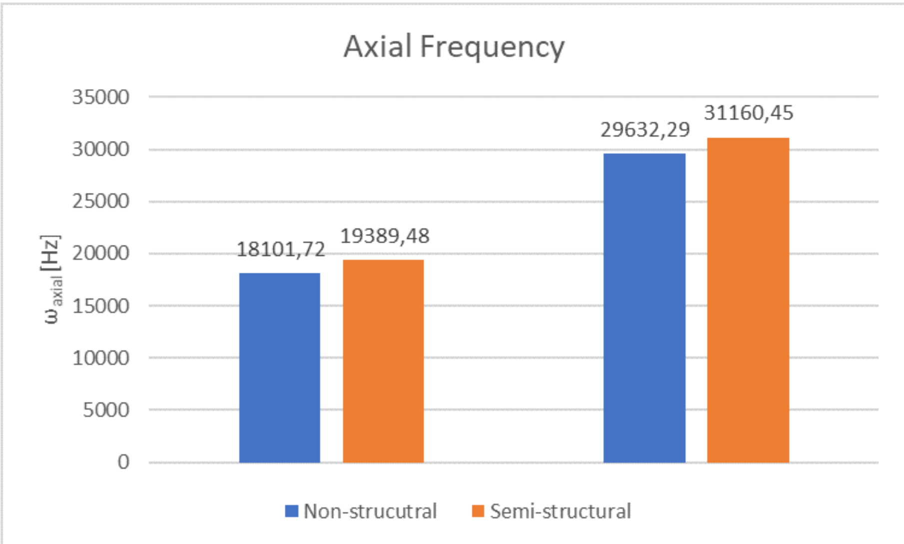

Figure 3.23: *Axial frequencies comparison*

an increase in axial frequencies for the semi-structural rotor model of 7% for the first one and of the 5% for the second one. Thus, the modification of the modulus of elasticity, made to meet the experimental results of the flexural dynamics, does not create significant variations in the natural axial frequencies.

Unfortunately, since the natural axial frequencies are higher than 10000 Hz, it was not possible to verify them experimentally due to the absence of accelerometers capable of measuring at frequencies higher than 10000 Hz.

Nevertheless, the real axial frequencies probably are in the range of figure 3.23.

Chapter 4

Supported rotor

As discussed in chapter 2, the rotor is supported by bearings and O-Rings. In this chapter, the dynamic behaviour of the O-Rings have been first analysed. As well known, the O-Rings have a non-linear behaviour, with respect to the excitation frequency, in terms of stiffness and damping. Due to their non-linear behaviour, the o-rings have been characterized using a data-driven model found in literature [24]. To get a model that could be easily implemented in a finite element model, the data of the predictive model has been described through a Maxwell-Wiechert model. The fit between the data of the predictive model and the Maxwell-Wiechert model has been realized through a genetic algorithm. At this point, the supports' model is introduced in the previously validated finite element FEM model as a connection between the free-free rotor and the ground. This allows to study the dynamics of the supported rotor and to obtain the critical speeds, the poles of the system and the unbalance response. These aspects are of fundamental importance in order to prevent unwanted vibrations of the system that can bring to undesired failure. Tests in rotation allowed to obtain the waterfall and it is noted that the first critical speed is very similar to the one computed from the model. Finally, to reach the target speed at 150000 rpm the rotor balancing has been performed, however it was not possible to reach the target the speed due to some problems linked with the inverter.

4.1 O-Rings dynamic behaviour

The O-Rings are rings made of visco-elastic material, like nitrile butadiene rubber (NBR), that are commonly used in mechanical applications both as gaskets and as passive energy dissipation devices. In this work, the O-Rings are used as passive energy dissipation devices: they are of fundamental importance since they damp the vibration of the rotor due to unbalance.

In a visco-elastic material the stress (σ) is not only dependent on the instant values of strain (ϵ) and velocity but it is also dependent on their past history. The most general model to describe this condition is the one reported in [25]:

$$\sigma = \int_{-\infty}^{t} E(t-\tau)\dot{\epsilon}(\tau)d\tau \tag{4.1}$$

Applying the Laplace transform to equation 4.1, the equation 4.2 is obtained.

$$\sigma(s) = E(s)\epsilon(s) = (E' + jE'')\epsilon(s) \tag{4.2}$$

Equation 4.2 is equivalent to equation 4.1 expect for E that is complex. This expression refers to the characteristics of the material and to make an analysis at the component level, the following expression can be found:

$$F(s) = k(s)x(s) = (k' + jk'')x(s) \tag{4.3}$$

where $x(s)$ is the component displacement and F is the reaction force.

Thus, from the equation 4.3 it is evident that the visco-elastic components are fully characterized with the determination of a complex stiffness k.

In general the dynamic properties of visco-elastic materials, such as the complex stiffness, are predicted by collecting experimental data [26]. Since in this thesis it has not been possible to carry out experimental tests, the O-Rings were characterized using the data-driven model proposed in [24].

This initial step allows collecting necessary information to perform the identification of the model's parameters, presented in section 4.3.

4.2 O-Rings data-driven model

The model proposed in [24] allows to find the real and imaginary part of the complex stiffness in the frequency range between 1.5 and 3.75 kHz, for O-Rings made with NBR and having a shore hardness of 70 and 90.

The model is based on experimental measurements, that are then generalized to obtain the real and imaginary part of the stiffness as function of three main parameters:

1. Ratio of diameter d/D;

2. Squeeze δ;

3. Shore hardness (Sh);

In this work the used O-Rings are made with NBR 70, while the calculation of both the squeeze and the ratio of diameter is based on the dimensions reported in the table 4.1.

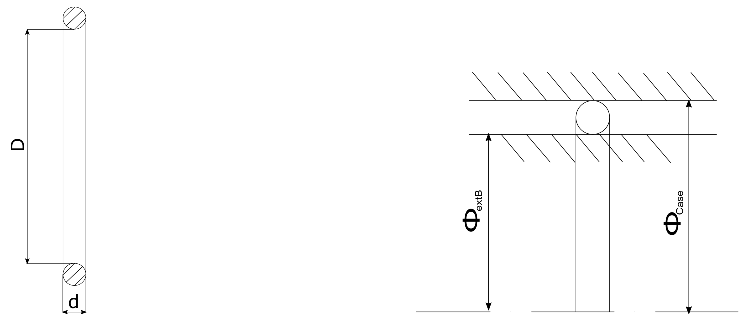

(a) *OR* **(b)** *Case*

Figure 4.1: *OR and Case nomenclature*

Table 4.1: *Or and Case dimensions*

D	19 mm
d	1.78 mm
Φ_{extB}	19 mm
Φ_{Case}	22.24 mm

The squeeze and the ratio of diameters can be calculated with equations 4.4 and 4.5

$$\delta = \frac{d - \frac{1}{2}(\Phi_{Case} - \Phi_{extB})}{d} = 9\% \tag{4.4}$$

$$d/D = 10.67 \tag{4.5}$$

4.2.1 Stiffness model

The real part of the complex stiffness (k' in equation 4.3) is the actual stiffness of the material and, according to the model, can be found from the adimensional stiffness $\underline{k}$ (Eq. 4.6) once E' and D are known.

$$\underline{k} = \frac{k'}{E'D} \tag{4.6}$$

Referring to the NBR with Sh of 70, the real part of the complex storage modulus (E') can be found as:

$$\log(E') = 0.259\log(f) + log(E'_0) \tag{4.7}$$

where E'_0 is the static storage modulus that can be found applying equation 4.8.

$$E'_0 = \frac{1-\mu^2}{2RC_3}\frac{C_1 + C_2Sh}{100 - Sh} \tag{4.8}$$

where $\mu = 0.47$ is the Poisson ratio and the others constant are R=0.395 mm $C_1 = 0.549$N, $C_2 = 0.07516$N, $C_3 = 0.025$mm as described in [27]. Finally, the adimensional stiffness can be calculated with formula 4.9:

$$\underline{\mathrm{k}} = a_0 + a_1\delta^{a_2} + a_3\left(\frac{d}{D}\right) \tag{4.9}$$

and the coefficients are determined experimentally by the model, and they reported in table 4.2.

Table 4.2: *Coefficient for* $\underline{k}$

a_0	0.9198
a_1	0.0624
a_2	1.123
a_3	-1.328

By combining the formulas 4.6, 4.7, 4.8 and 4.9 it is possible to obtain k' (Fig 4.2).

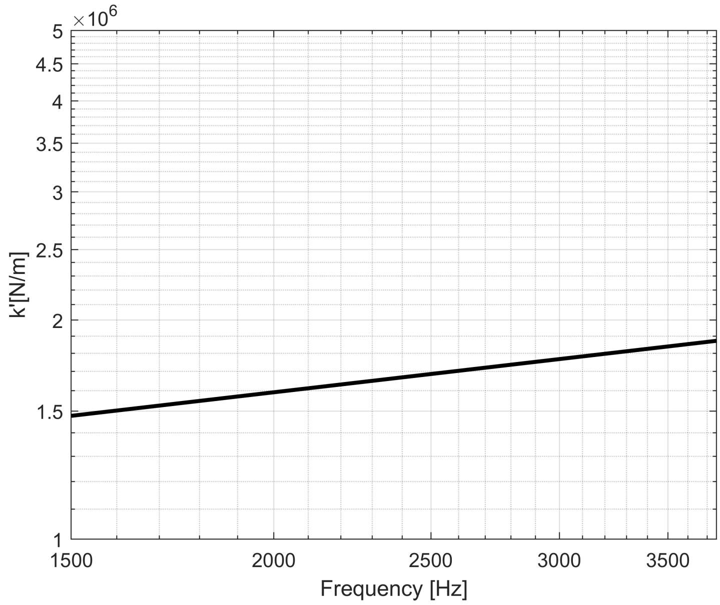

Figure 4.2: *In-phase component of the reduced-order model*

4.2.2 Damping model

The imaginary part of the complex stiffness (k'' in equation 4.3) is the damping capability of the material and, according to the model, it can be found from the definition of loss factor:

$$\eta = \frac{k''}{k'} \tag{4.10}$$

The reduced-order model in [24] provide the following expression for η:

$$\eta = a_0 + a_1 f + a_2 f^2 \tag{4.11}$$

where the coefficients are determined experimentally by the model, and they reported in table 4.3.

Table 4.3: *Coefficient for η*

a_0	0.1811
a_1	2.372 x 10^{-04}
a_2	-5.261 x 10^{-08}

The in-quadrature k'' is reported in figure 4.3.

At this point the dynamic of the O-Rings is completely characterized in the frequency range between 1.5 and 3.75 kHz.

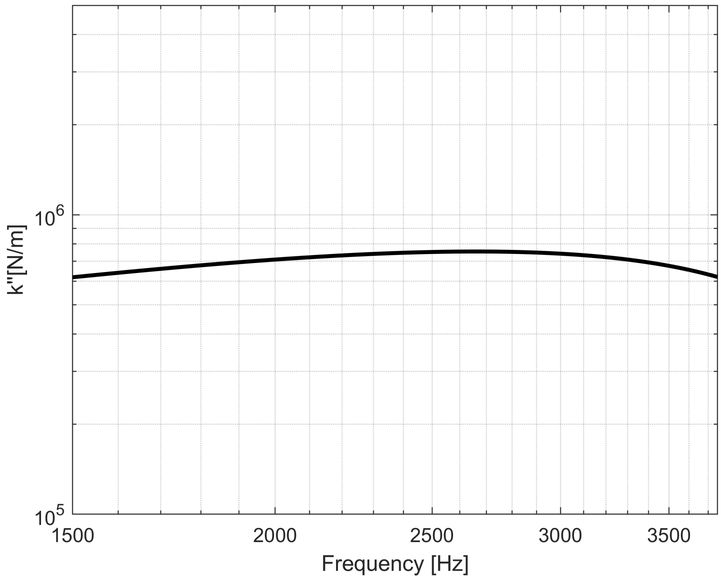

Figure 4.3: *In-quadrature component of the reduced-order model*

Despite the good approximation,the non-linear equations of the data-driven model do not allow to easily represent it in the finite element model of the shaft. Thus, to overcome this problem and to implement the O-Rings' dynamics in the rotor model, only linear elements are used. This second approach is presented in the following section and the results of the data-driven model have been used as reference.

4.3 Maxwell-Wiechert model

The dynamic behaviour of the O-Rings can be described with different type of models, as described in [28]. All the models can be grouped into:

1. Rheological models (Maxwell–Wiechert, fractional derivative etc..);

2. Complex modulus model;

In this work the Maxwell–Wiechert model (figure 4.4) is considered. This model describes the behaviour of the material using springs and dampers in series. The number of springs and dampers does not have a precise physical meaning but it still allows both to have a good approximation of the visco-elastic material behaviour and to be easily implemented in a finite element model.

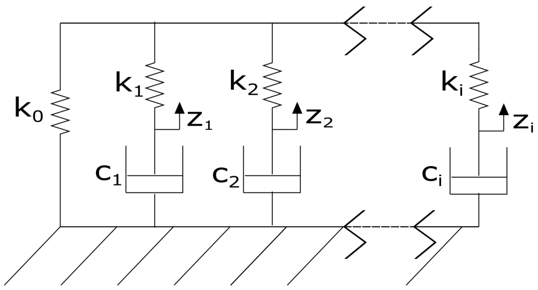

Figure 4.4: *Maxwell - Wiechert model*

The force of a Maxwell-Wiechert model with n branches depend on the traction/-compression x applied to the material and it is equal to:

$$F = \left(k_0 + \sum_{i=1}^{n} \frac{k_i s}{s + \frac{k_i}{c_i}} \right) x \tag{4.12}$$

In the equation 4.12 it is possible to observe the presence of a complex stiffness.

In particular, the real part is in-phase and it is proportional to the actual stiffness of the material, while the imaginary part is in quadrature and it is proportional to the capacity of the component to dissipate energy, i.e. the damping capability.

In this work the Maxwell-Wiechert model with two branches was used. The expression of the complex stiffness is reported in eqation 4.13:

$$K = \frac{F}{x} = k_0 + \frac{k_1 s}{s + \frac{k_1}{c_1}} + \frac{k_2 s}{s + \frac{k_2}{c_2}} \tag{4.13}$$

4.4 Parameters identification with Genetic Algorithm

The real and imaginary part of the stiffness determined with the data-driven model are compared to the real and imaginary part of the equation 4.13 in order to identify the values of k_0, k_1, c_1, k_2 and c_2. The identification is performed by means of a Genetic Algorithm (GA), aiming to minimize the difference between the results of the data-driven model and the results provided by the equation 4.13.

Genetic algorithms (GA) are heuristic, search-based algorithms based on the concept of natural selection [29]. These algorithms are frequently used in optimization problems to find the optimal or near-optimal solution [30].

The working principle of the genetic algorithm is based on the recombination and mutation of the possible solutions, called *chromosomes*. The *chromosomes* represent the codification of all the parameters of the solution, and they are expressed with a binary string in which each element is called *gene*. The *chromosomes* are compared each other through the evaluation of the *fitness function* that indicates the quality of the solution. This process is repeated over various generations until the *fitness function* is optimized. The *population* is the set of *chromosome*. The first population is generated randomly while the following ones are generated, starting from the previous, by means of genetic operations like *selection, cross-over, ellitism and mutation.*

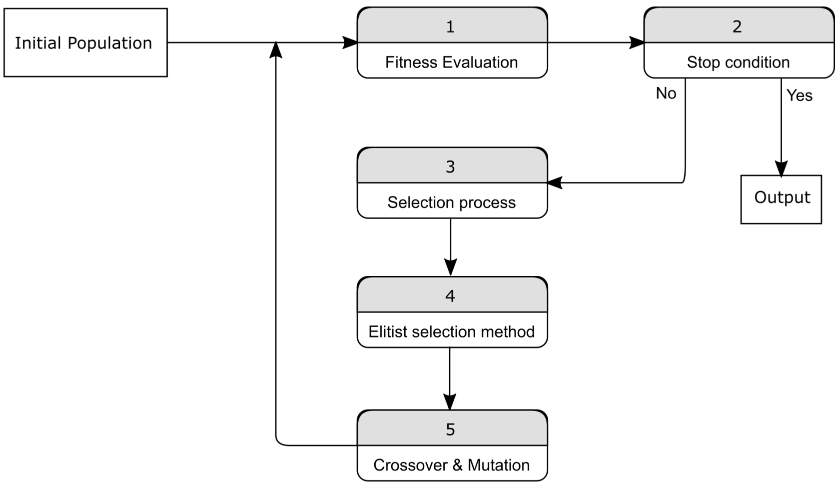

Figure 4.5: *Flow chart of GA*

Selection Process

The selection process can be done with different techniques [26], like *Tournament Selection, Normalized Geometric Selection, Roulette Wheel Selection*. In this work the *Roulette Wheel Selection* has been used.

In this type of selection process each individual can become a parent for the next generation with a probability which is proportional to its fitness. Let's consider a pie (figure 4.6) divided in a number of parts equal to the number of chromosomes in the population. Each chromosome has a part of the pie proportional to its fitness. A selection point has been set on the wheel. At this point the wheel is turned and the chromosome that is closest to the selection point when the wheel stops is the first parent of the next generation. For the second parent the same procedure is repeated and so on.

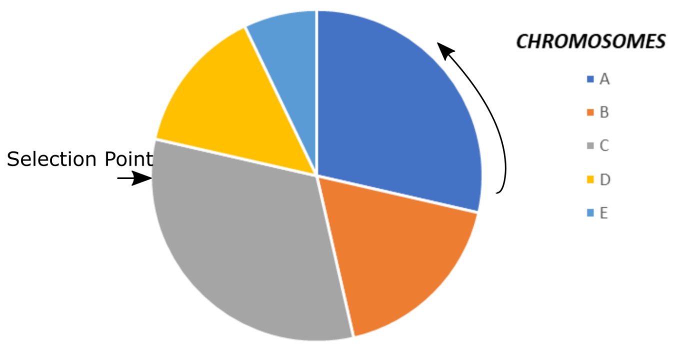

Figure 4.6: *Roulette Wheel Selection*

Elitist Selection Method

The elitist selection method saves a copy of the best element of each population before the production of the next generation. In this way it is ensured the survival of the best element of each population.

Cross-Over Procedure

The cross-over procedure allows the creation of new individuals from the genetic material of the parents. It consists in the swapping of the chromosomes of the parents in order to generate children. This allows the generation of the new population. In figure 4.7 it is depicted the One Point cross-over.

Figure 4.7: *Cross-Over*

Mutation Procedure

The mutation is a stochastic procedure that flips the binary values of the chromosomes. This allows avoiding sub-optimal convergence of the solutions.

0	1	0	0	1	1	0
0	0	0	1	1	1	0

Figure 4.8: *Mutation*

Parameters Identification

In the proposed GA, each chromosome of the population is encoded as a vector of real numbers that contain the stiffness and the damping coefficients of each branch:

$$C = [k'_1, c'_1, k'_2, c'_2] \tag{4.14}$$

For each element of the chromosome it is necessary to define an upper and lower bound, reported in the table 4.4.

Table 4.4: *Upper and lower bound of the chromosomes*

	$k'_1[N/m]$	$c'_1[Ns/m]$	$k'_2[N/m]$	$c'_2[Ns/m]$
min	1×10^2	1×10^1	1×10^2	3×10^3
max	5×10^6	1×10^2	1×10^6	4×10^3

The fitness function F_{obj} is formulated in order to have a significant measurement of chromosomes quality. The difference between the value of the real parts and that of the imaginary parts of the reduced-order model and the Maxwell-Wiechert model is considered as the error. This difference is then considered in the calculation of the Mean Square Error (MSE). Since the algorithm maximizes an objective function, it is necessary to define it as the reciprocal of the MSE, as in equation 4.15.

$$F_{obj} = \frac{1}{W_{Re}\left(\frac{\sum_{i=1}^{n}(Re(K)-k')^2}{n}\right) + W_{Im}\left(\frac{\sum_{i=1}^{n}(Im(K)-k'')^2}{n}\right)} \tag{4.15}$$

where n is the size of the frequency vector, W_{Re} and W_{Im} are the weighting coefficients for the real and the imaginary part, and they are set, respectively, 0.5 and 1. The GA is implemented with a population of 40 individuals in 200 generations.

To run the code it is necessary to fix a value for the static stiffness k_0 and it has been fixed, with a trial and error procedure, to $2.25 \times 10^5 N/m$. The identified parameters are reported in the table 4.5.

Table 4.5: *Maxwell-Wiechert model parameters*

$k_1[N/m]$	$c_1[Ns/m]$	$k_2[N/m]$	$c_2[Ns/m]$
1.42×10^6	86.47	7.88×10^5	3.03×10^3

In Figure 4.9 is reported the convergence plot. It is possible to observe that all the parameters converge to the values identified as the best.

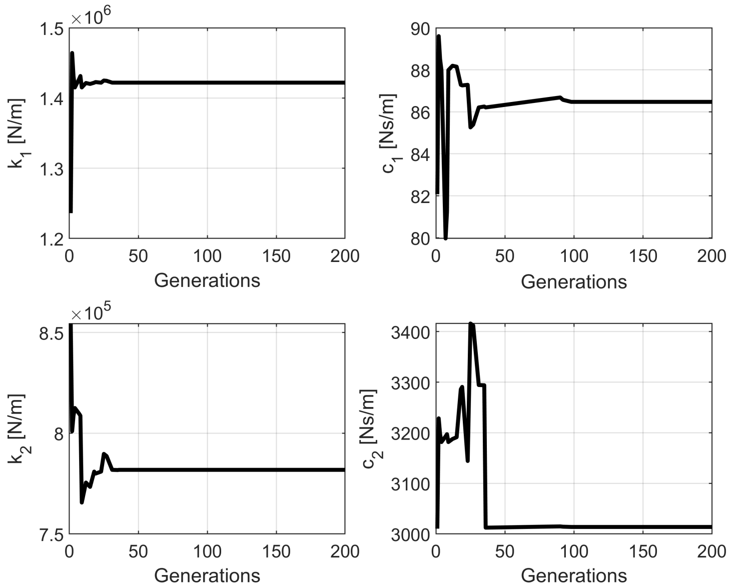

Figure 4.9: *GA convergence*

With these parameters, the real k' and the imaginary part k'' of the complex stiffness is depicted in figure 4.10.

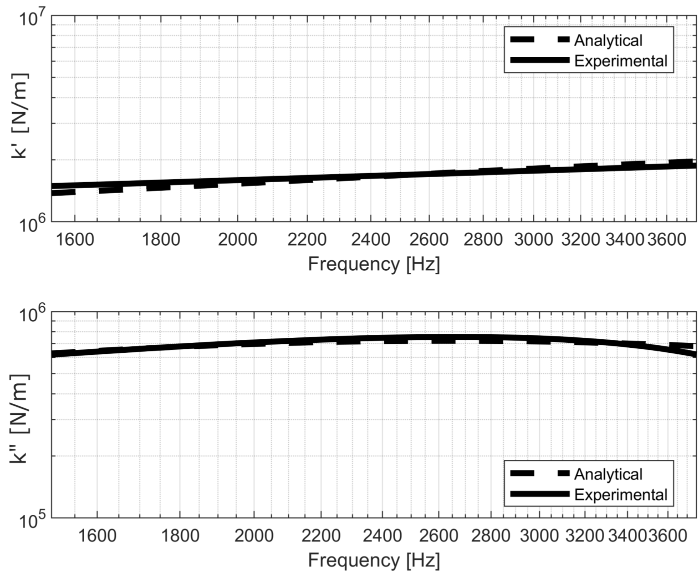

Figure 4.10: *Model fit*

The interpolation obtained is satisfying, for this reason it has been chosen to use the Maxwell-Wiechert model not only in the frequency range used for interpolation but also at lower frequencies. Extending the Maxwell-Wiechert model to lower frequencies it has been obtained the trend of figure 4.11.

The red area is the one in which the data are interpolated, while the green area is the one in which the model has been extended.

The elastomeric support provides a low value of stiffness and damping at low frequencies. At high frequencies the stiffness converges to a maximum value while the damping starts to decrease.

In conclusion, it is important to highlight that the proposed identification does not consider the effects of temperature on the properties of the visco-elastic materials. In particular, the characterization of the O-Rings with respect to the temperature variation is out of the scope of this thesis.

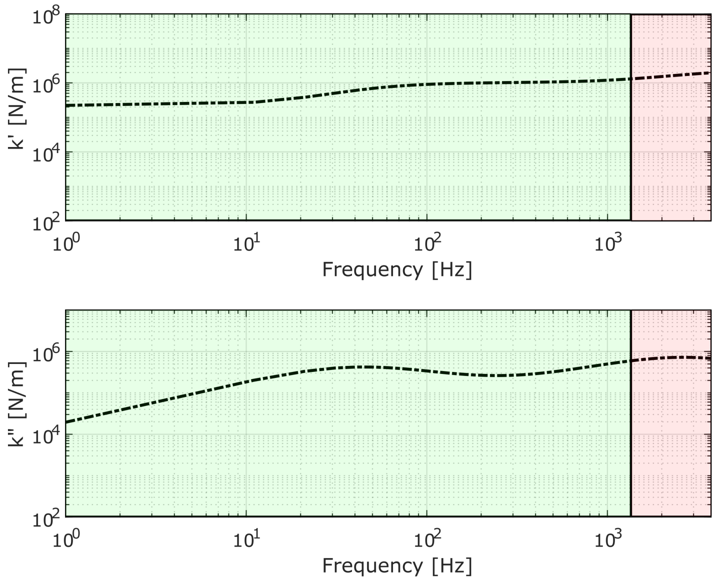

Figure 4.11: *Dynamic behaviour in the whole range of frequencies*

4.5 Rotordynamic analysis

To carry out the dynamic analysis of the rotor, the finite element model validated in chapter 3 has been connected to Maxwell-Wiechert model analysed in the previous paragraph.

4.5.1 FEM model

The FEM model of the supported shaft is reported in figure 4.12. The same mesh used for the free-free model has been used, so the complex DOFs associated with the shaft are 210 (206 associated with the beam elements plus 4 associated with the masses), plus 4 internal, complex DOFs associated with Maxwell-Wiechert model. All the DOFs have to be considered as complex, this allows to halve the dimension of the problem. The Maxwell-Wiechert model has been connected on the one hand to the ground, thus considering the stator as infinitely rigid, and on the other hand to a mass ($m_{bear} = 7\ g$), which represents the mass of the bearings, connected to the shaft by a spring that represents the spheres' stiffness (k_{sphere}). The stiffness of the bearings has been considered constant because it is certainly at least two orders of magnitude higher than the stiffness of the O-Rings and therefore its influence is non-negligible only at higher frequencies.

To connect the O-Rings to the shaft it was necessary to represent their dynamics in

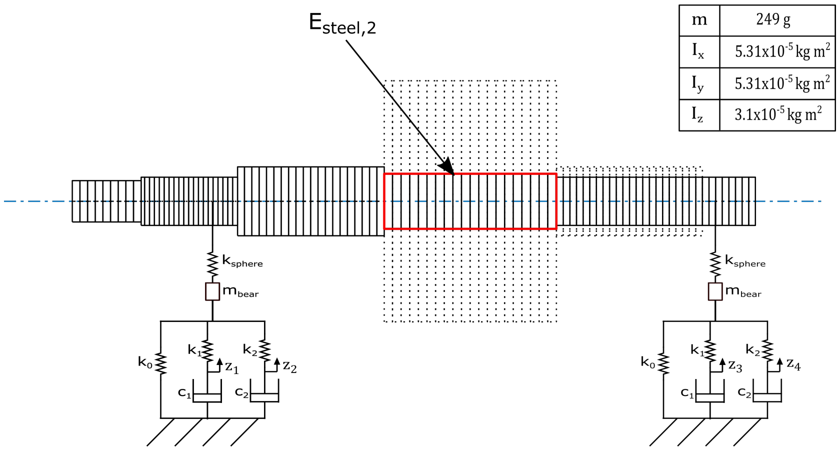

Figure 4.12: *FEM model of the supported rotor*

the state-space. This can be done considering as input the base displacement x, which corresponds to the one of the mass m_{bear}, and as output the force F that the O-rings apply on the mass.

$$\begin{Bmatrix} \dot{z}_1 \\ \dot{z}_2 \end{Bmatrix} = \begin{bmatrix} -\frac{k_1}{c_1} & 0 \\ 0 & -\frac{k_2}{c_2} \end{bmatrix} \begin{Bmatrix} z_1 \\ z_2 \end{Bmatrix} + \begin{bmatrix} \frac{k_1}{c_1} \\ \frac{k_2}{c_2} \end{bmatrix} x \tag{4.16}$$

$$F = \begin{bmatrix} -k_1 & -k_2 \end{bmatrix} \begin{Bmatrix} z_1 \\ z_2 \end{Bmatrix} + [k_0 + k_1 + k_2]x \tag{4.17}$$

Regarding the dynamics of supported shaft, the same equations reported in the section 3.2 has been used. The force F of the O-Rings is the input for the shaft while the output is the displacement of the masses m_{bear}.

Then, the connection between shaft and OR can be made by considering the scheme of figure 4.13.

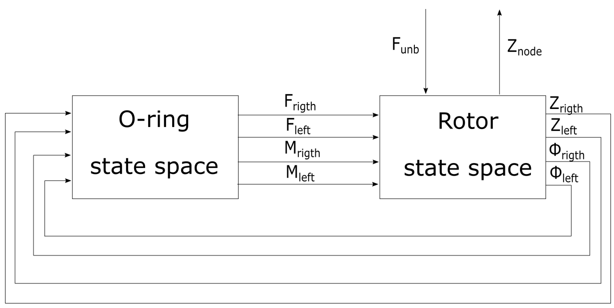

Figure 4.13: *Block diagram of the whole system*

Thus, the two different systems are coupled in order to get a single system. This connection is done with MATLAB.

The unique system allows the calculation of the system poles, critical speeds and unbalance response.

4.5.2 Numerical model results

The analytical results have been computed for a maximum rotor angular speed of 250000 rpm, even if the maximum speed of the rotor is 150000 rpm. This because it is important to verify that the first flexural critical speed is at least 20% higher than the maximum speed of the rotor.

System poles

The poles of the system are 428: 420 associated with the shaft and 8 associated with the Maxwell-Wiechert model. The poles of the system are the natural frequencies, and they are expected to be complex. The general form of the poles is the one reported in equation 4.18:

$$s = s_R + js_I \tag{4.18}$$

The real part (s_R) represents the decay rate of the systems: it is negative for a stable system and positive for an unstable one. The natural frequencies of the system are the imaginary part (s_I) of the poles. The real and imaginary part of the poles is shown in figure 4.14.

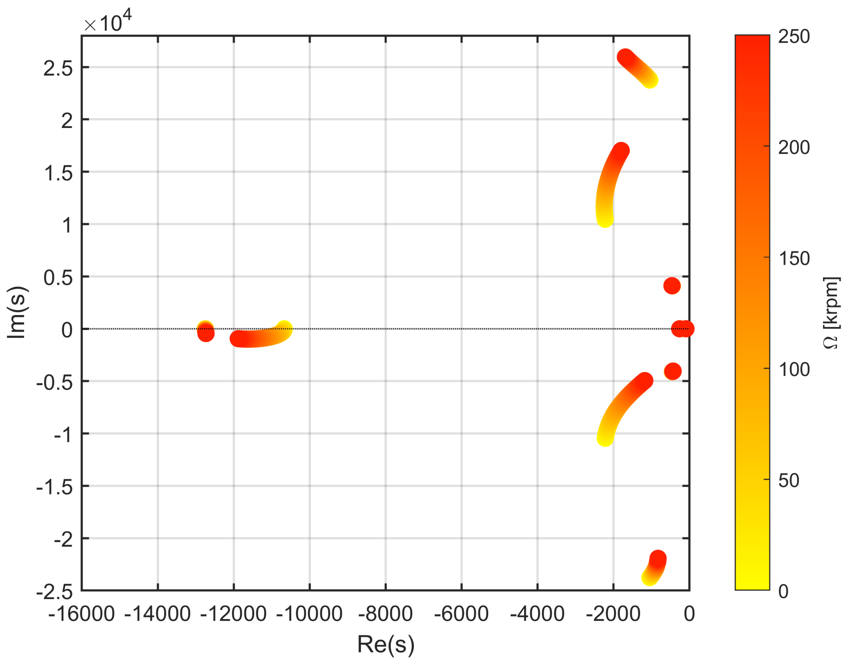

Figure 4.14: *Poles map*

The system is stable since all the poles have a negative real part. At $\Omega = 0$ the poles are complex and conjugates, while increasing Ω they loose this property due to the gyroscopic effect. At standstill the poles associated with the Maxwell-Wiechert model are real, this is correct since no mass is associated to the internal DOFs. When the speed increases, these poles acquire an imaginary part. In fact, the gyroscopic effect creates a coupling of the motion between the planes x-z and y-z.

Critical speeds

The critical speeds of the rotor can be found analysing the Campbell diagram, in which the natural frequencies of the system (imaginary part of the poles) are reported. The Campbell diagram is reported in figure 4.15.

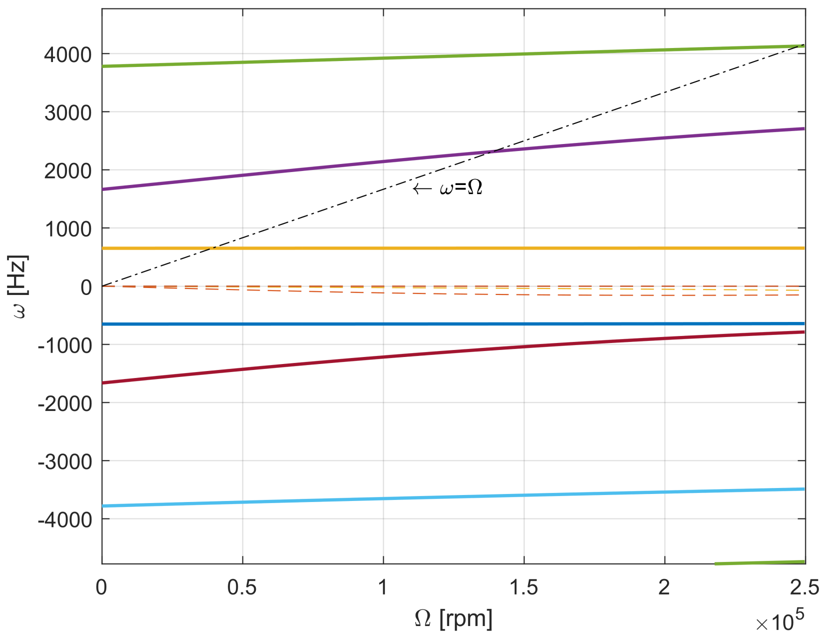

Figure 4.15: *Campbell diagram*

The intersections between the straight line $\omega = \Omega$, which represents the excitation due to unbalance, and the natural frequencies determine the critical speeds. The critical speeds are $\Omega_{cr1} = 45\ krpm$ and $\Omega_{cr2} = 137\ krpm$.

If the rotor rotates at one of these two speeds, strong vibrations on the rotor supports arise, while the deformation of the shaft is limited. This behaviour can be demonstrated analysing the form of the first two vibrating modes, which are shown in the figure 4.16. These two modes are exclusively linked to the supports' stiffness, and

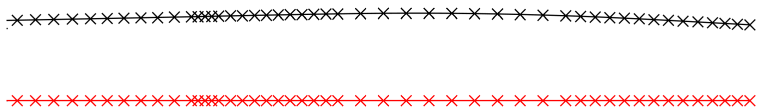

(a) *Mode 1 at 750 Hz*

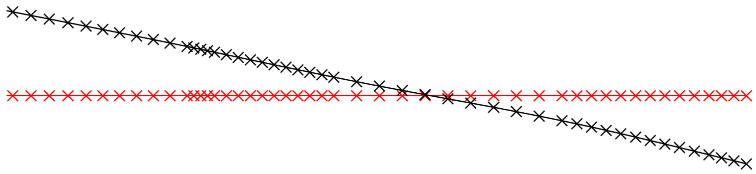

(b) *Mode 2 at 1664 Hz*

Figure 4.16: *Modal shapes*

therefore the frequency at which they occur is a function of it.

To operate in safety condition the first flexural critical speed must be outside the safety margin region of the 20% with respect to the maximum rotational speed [7] (i.e. 1^{st} flexural critical speed > 180000 rpm).

In this case the first flexural critical speed is at $\Omega_{cr3} = 250\ krpm$, so the rotor works within the safety region. The related mode shape is the one in figure 4.17.

Figure 4.17: *Mode shape of the first flexural natural frequencies*

Unbalance response

The unbalance response has been calculated considering a balance grade of 9. This balance grade is considered good for this type of application [22]. The maximum displacement due to the unbalance is reported in figure 4.18 and it is located in the node 1 of the shaft.

The displacement of the shaft is very small, so only a little amount of vibration should arise at high speed. Thus, the rotor can operate safely without any kind of structural problem that could lead to a sudden failure of the prototype.

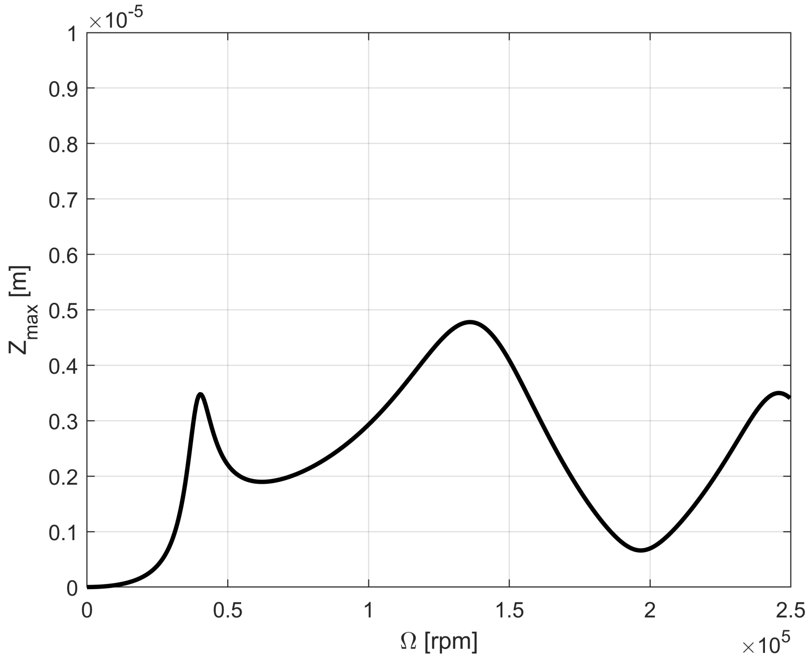

Figure 4.18: *Unbalance response*

The satisfying numerical results allow moving on experimental test at high rotational speed.

4.6 High-speed experimental test

The test bench in Figure 4.19 is designed to characterize the hysteresis machine as a motor up to the typical speeds of use of a turbocharger, in this case up to 150000 rpm. The prototype (Figure 4.20a) is placed inside a steel safety cell and fixed to a seismic mass by means of brackets. From a lubrication point of view, each cover has an inlet and outlet for the distribution of an air-oil mixture to the two bearings supporting the rotor. The inlet and outlet lines are in turn connected to the lubrication system shown in Figure 4.20b.

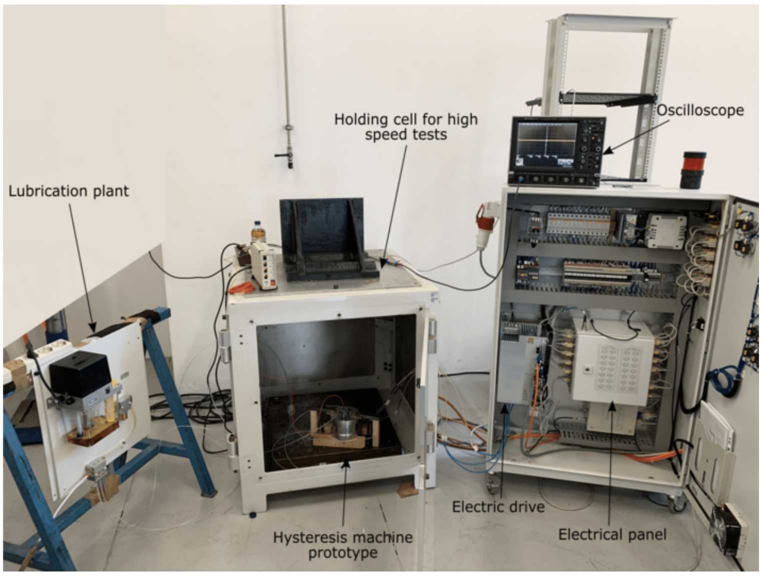

Figure 4.19: *High-speed test bench*

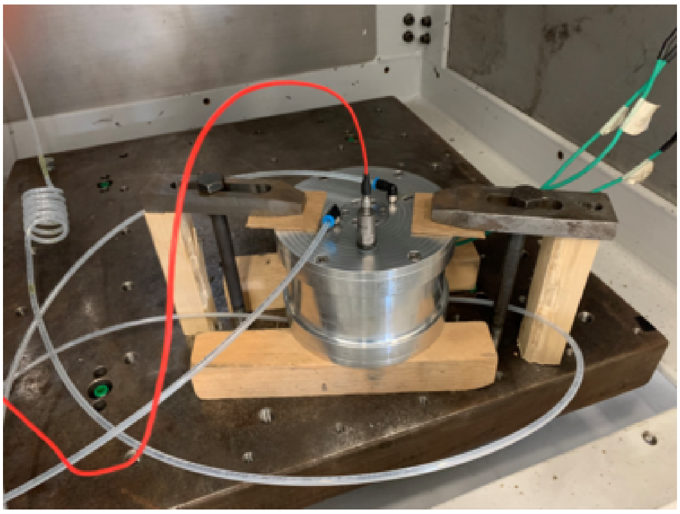

(a) *Hysteresis machine prototype mounted in the safety cell*

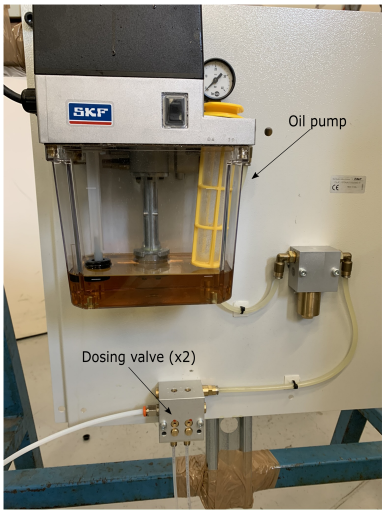

(b) *Lubrication plant*

Figure 4.20: *Test bench components*

4.6.1 Lubrication

An air-oil system is used for the lubrication of the bearings. This choice is due to the high rotation speeds achieved in this application. This type of lubrication has some advantages like the reduction of lubricant consumption, contact area protection, prevention of abrasion and skidding and it is also environmental friendly since no oil mist or fog is created. In air-oil lubrication, a flow of compressed air separates a certain flow of lubricant, generating streaks that travel along the walls of the pipes. This mixture reaches the rolling elements of the bearing through the hole in the outer ring. A second hole is used to evacuate the lubricant and avoid accumulation inside the bearing. The lubrication system consists of:

1. Oil control unit 0.1 lt/min 30 bar
2. Supporting plate
3. Air+oil mixer $2 \times 0.01cm^3$
4. Flexible polyamide pipe

Since the control unit is not present, it is necessary to install a switch to manually control the pump operating interval within each lubrication cycle of duration. The operating time is calculated from the oil flow rate required by each bearing, obtained from the empirical formula provided by SKF.

The lubrication system is continuously supplied with compressed air at 7 bar. The mixer is equipped with valves for the regulation of the air flow. This is set in such a way that the oil line in the pipe proceeds at a speed of about 1 m/s, as recommended by SKF technicians.

The control unit can work with oils ranging from an ISO VG-32 to an ISO VG-100. Due to the particularly high rotation speed, it is decided to use an ISO VG-32 in this application. Using this oil, a complete film lubrication regime is always ensured, so that the contact load is borne by the lubricant. This improves the working conditions of the bearing and extends its life.

4.6.2 Test description

A preliminar test without balancing the rotor has been performed powering the hysteresis machine with an industrial Kollmorgen Servostar S748 drive. This applies a voltage/frequency (V/f) ramp control strategy that can drive the machine in an open loop. Since the strategy applies three-phase voltages without position feedback, the addition of an accelerometer is necessary to understand the motor speed by measuring the vibration of the cover.

The machine is driven at increasing speed with an acceleration ramp of 314.16 rad/s^2, thus reaching a maximum speed of 80 $krpm$. Smaller acceleration ramp (60 rad/s^2) and a maximum speed of 60 $krpm$ led to the synthesis of waterfall diagram shown in figures 4.21 and 4.22.

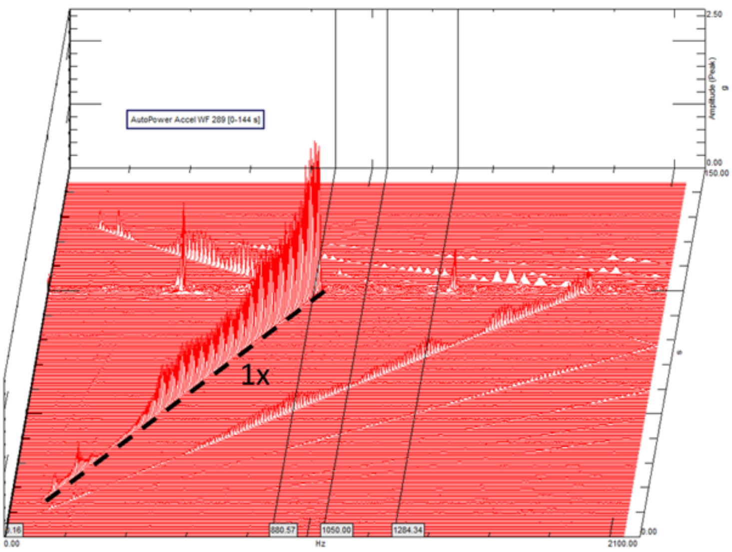

Figure 4.21: *3D waterfall diagram obtained for speeds from 0 to 60 krpm*

From the waterfall diagram it is possible to identify the first critical speed of the system, that, according to the numerical model, is between 45000-50000 rpm.

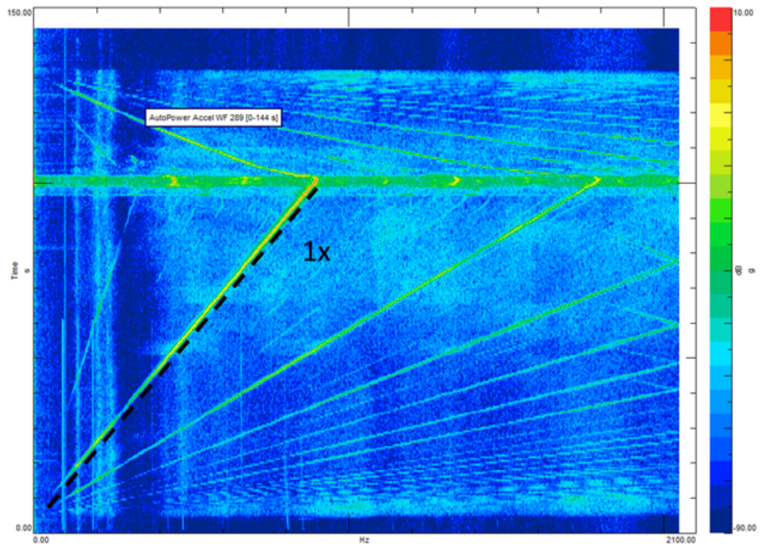

Figure 4.22: *Colour-map waterfall diagram obtained for speeds from 0 to 60 krpm*

From the experimental response it is evident that the unbalance grade of the rotor is much higher than 9, so the target speed of 150000 rpm cannot be reached. Thus, the rotor has been balanced, at least to reach a balance grade of 9.

4.7 Rotor balancing

Rotor balancing is a highly specialized technology aimed at balance rotor before they started their service life.

Since the rotor works far from its first flexural critical speed, it can be considered *rigid*. Thus, the balancing procedure for rigid rotors has been followed.

A rigid rotor can be balanced adding or removing mass on two planes perpendicular to the axis of rotation. In this case, since there isn't enough space for adding mass, it has been decided to design two disks from which removing mass. The balancing disk and the bushing used for centring are reported in figure 4.23. The bushings are

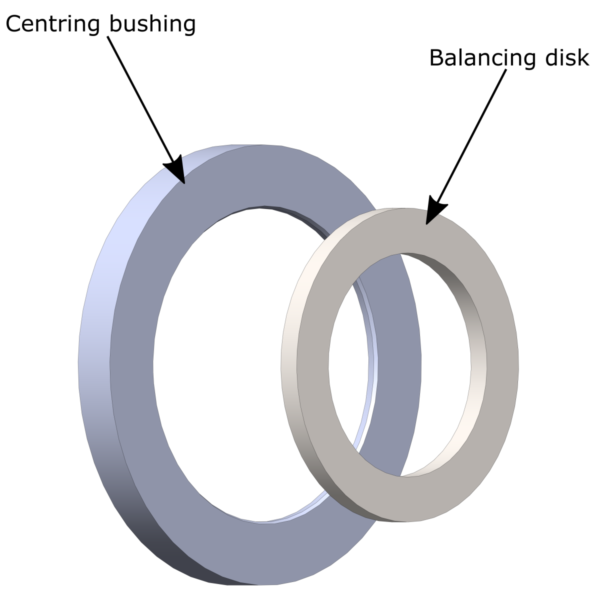

Figure 4.23: *Balancing disk and centring bushing*

used to centre the balancing disks on the two sides of the electric machine rotor, their outer diameter is 35 mm, while their inner diameter is 28 mm. The disks are glued to both the sides of the electric motor, they have an inner diameter of 20 mm, an outer diameter of 28 mm, and a thickness of 2 mm. The disks are glued with the same procedure used for the CROVAC sheets, reported in the section 2.3. After gluing these two discs, the centring bushing has been removed. The mounting scheme of the balancing disk is reported in figure 4.24.

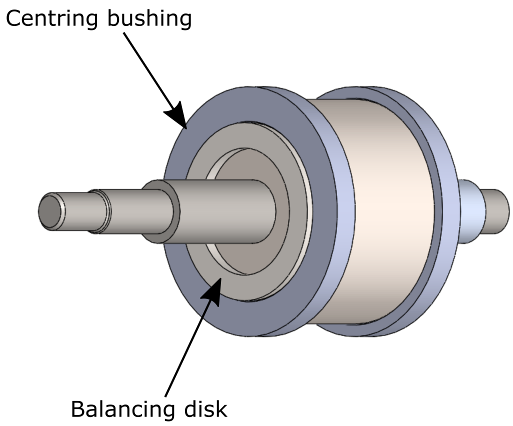

Figure 4.24: *Disks mounting*

The two glued disks have been used as the two planes perpendicular to the axis of rotation that are needed for the balancing procedure. A scheme of that is reported in figure 4.25.

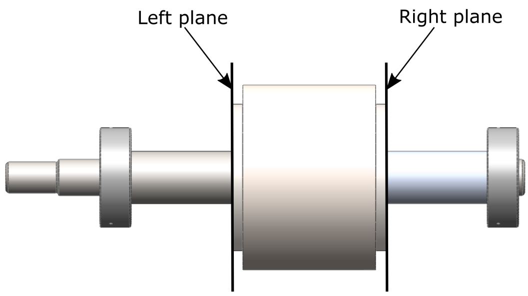

Figure 4.25: *Reference planes*

4.7.1 Balancing procedure

Since the rotor has been considered rigid, its dynamic behaviour is defined with 2 complex DOF, in this case they are the displacement of the two reference planes.

The balancing procedure has been done at Elettrorava spa. The machine used for balancing (figure 4.26) is a low-stiffness machine that measures the displacement of the rotor on the two reference planes.

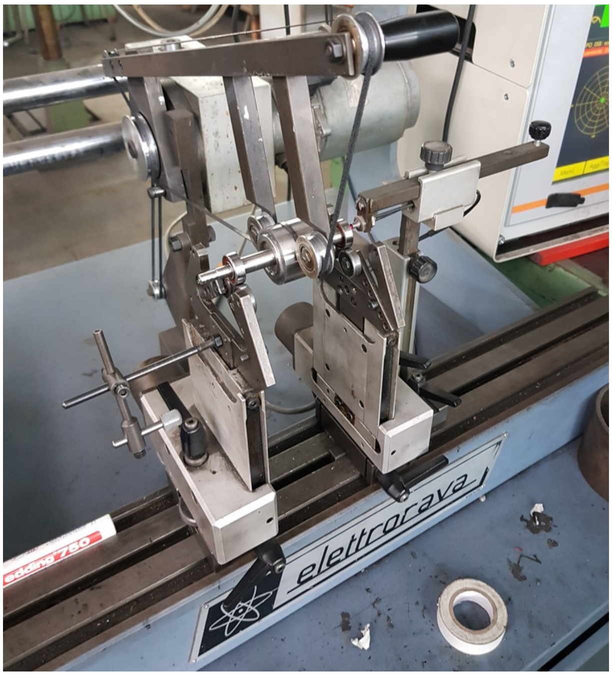

Figure 4.26: *Balancing machine*

Being the rotor considered as rigid the equation of motion is the following:

$$[M]\{\ddot{q}\} + (-j\Omega[G] + [C])\{\dot{q}\} + [K]\{q\} = \{F_{unb}\}e^{j\Omega t} \tag{4.19}$$

where q is a 2x1 vector containing the displacement of the DOFs, i.e. the displacement of the two reference planes. $\{F_{unb}\}$ is a 2x1 vector containing the unbalance on the reference planes. The aforementioned terms are complex.
The general solution of the equation is:

$$\{q\} = \{q_0\}e^{j\Omega t} \tag{4.20}$$

where the components of $\{q_0\}$ are complex.
Substituting equation 4.20 and its derivatives into equation 4.19:

$$(-[M]\Omega^2 + \Omega(\Omega[G] + j[C]) + [K])\{q_0\}e^{j\Omega t} = \{F_{unb}\}e^{j\Omega t} \tag{4.21}$$

that can be simplified in:

$$\{q_0\} = [R(\Omega)]\{F_{unb}\} \tag{4.22}$$

where $[R(\Omega)]$ is the receptance matrix (2x2), $\{q_0\}$ is a 2x1 vector that contains the complex displacement of the rotor on the two reference planes and $\{F_{unb}\}$ is the un-

balance of the rotor on the two planes.
In this way, knowing the matrix R and the unbalance it is possible to know the displacement of the DOFs.

The followed balancing procedure can be divide in 4 step:

Step 1

A free run of the rotor at constant spin speed Ω has been performed. The machine measures the displacement on the two planes that is linked to the original unbalance by the following relation:

$$\{q_0\} = [R(\Omega)]\{F_{unb0}\} \tag{4.23}$$

where $\{F_{unb0}\}$ is the initial unbalance of the rotor, that is unknown.

Step 2

In this step the calibration of the machine has to be performed, this means that the receptance matrix $[R(\Omega)]$ has to be defined.

To do this, a trial mass has been added to each plane, on the outside diameter of the disk, in turn. This procedure allows to add a known unbalance on the rotor, so the total unbalance is the original plus the added one.

Adding the mass on the first plane and performing a run at the same spin speed (Ω), the measured displacement is:

$$\{q_1\} = [R(\Omega)]\{F_{unb0}\} + [R(\Omega)]\{F_{unb1}\} = \{q_0\} + [R(\Omega)]\{F_{unb1}\} \tag{4.24}$$

If the mass is added to the second plane and a spin at Ω is performed, the measured displacement is:

$$\{q_2\} = [R(\Omega)]\{F_{unb0}\} + [R(\Omega)]\{F_{unb2}\} = \{q_0\} + [R(\Omega)]\{F_{unb2}\} \tag{4.25}$$

Defining $\{q_{d1}\}$ and $\{q_{d2}\}$ as $\{q_1\} - \{q_0\}$ and $\{q_2\} - \{q_0\}$ respectively the equations 4.24 and 4.25 can be organized in the following matrix format:

$$[\{q_{d1}\}\{q_{d2}\}] = [R(\Omega)][\{F_{unb1}\}\{F_{unb2}\}] \tag{4.26}$$

From equation 4.26 the receptance matrix $[R(\Omega)]$ can be found as:

$$[R(\Omega)] = [\{q_{d1}\}\{q_{d2}\}][\{F_{unb1}\}\{F_{unb2}\}]^{-1} \tag{4.27}$$

Substituting this equation in 4.23 the original unbalance of the system can be found:

$$\{F_{unb0}\} = -[\{F_{unb1}\}\{F_{unb2}\}][\{q_{d1}\}\{q_{d2}\}]^{-1}\{q_0\} \tag{4.28}$$

where, $\{F_{unb0}\}$ is a 2x1 complex vector.

Step 3

The mass that has to be added or removed can now be calculated as a function of the radius at which it will be removed:

$$\begin{aligned} m_1 &= \frac{|F_{unb0}(1)|}{r_1} \\ m_2 &= \frac{|F_{unb0}(2)|}{r_2} \end{aligned} \tag{4.29}$$

while the angular position at which the mass has to be removed is the phase of the $F_{unb1} + 180°$.

This procedure is automatically performed by the balancing machine and as output it gives the mass that has to be removed on the outer diameter of the balancing disk. The mass that has to be removed at this stage is 142 mg at 37° on the outer diameter of the left balancing disk and 160 mg at 240° on the outer diameter of the right balancing disk.

Step 4

The steps have to be repeated until a satisfying balance has been obtained.

At the end of the procedure the modulus of the remaining unbalance is 1.4×10^{-7} kgm on both the planes. From this value it is possible to calculate the balancing grade G, as defined by the ISO 1940:

$$G = \Omega_{max}\epsilon = \Omega_{max}\frac{1.4 \times 10^{-7}}{m_{tot}} = 9mm/s \tag{4.30}$$

where $m_{tot} = 244.6g$ is the whole mass of the rotor.

The final balance grade obtained with this process is 9. This value is satisfying, even if the ISO 1940 suggests G = 2.5 for this type of applications. However, to reach the suggested balance grade a mass of 8 mg should be removed on the rotor, this can be done only with an high precision instrumentation that is not available.

4.8 High speed test with balanced rotor

After carrying out the balancing procedure of the rotor, it has been tried to bring it to the speed of 150000 rpm. For a more accurate speed estimation, the reflective object sensor *tt electronics OPB703WZ* has been mounted on the machine cover, near the shaft. The installation of the sensor is reported in figure 4.27.

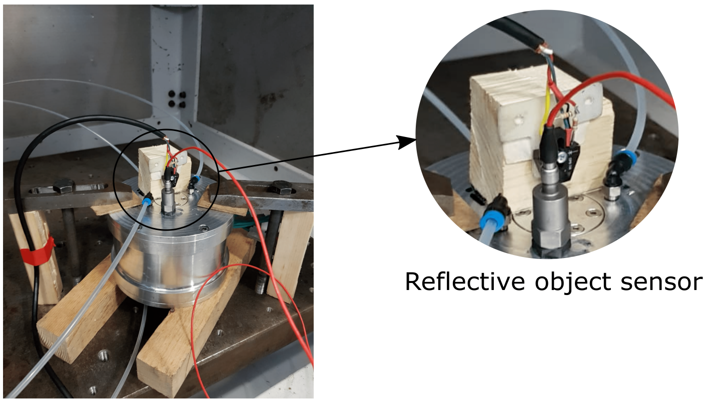

Figure 4.27: *Balancing machine*

The working principle of this sensor is reported in figure 4.28.

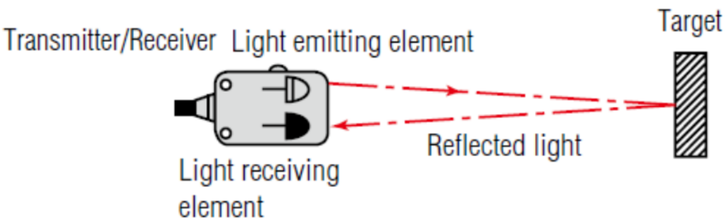

Figure 4.28: *Balancing machine*

It is composed by a element that emits light and by an element that receive light. When a reflective surface passes in front of the sensor a nil tension is produced as output. Instead, when a non-reflective surface passes in front of the sensor a tension of 5 V is produced. So, it is possible to measure the angular speed of an object dividing its surface in a reflective and a non-reflective part. In this way, the sensor produces a square wave output, and the frequency of the square wave is the angular speed of the shaft. To do this on the analysed shaft, half of its surface that comes out from the stator has been coloured black, so it is non-reflective, while the other part of the shaft reflects the light.

The signal coming from the optical sensor has been put as reference in the acquisition, while the other input is the signal coming from the accelerometer positioned on the cover.

It was not possible to reach the target speed of 150000 rpm, since a firmware upgrade of the inverter limits the speed that can be reached in sensorless operation at 599 Hz. This limitation is due to safety reasons.

Besides the problems with the inverter, the satisfying numerical results (i.e. the small displacement reported in figure 4.18) allow trying to reach the target speed of 150000 rpm without mechanical problems.

Chapter 5

Conclusion and future works

This research aimed both to mechanically design the rotor of a hysteresis machine for electric turbo-compound and to analyse its dynamic behaviour. Based on the high centrifugal forces involved at 150000 rpm, it was fundamental both to accurately design the rotor and to study its dynamic behaviour.

The rotor material was chosen after some tensile tests on different SHMMs. The material that allowed reaching high speed, having at the same time good magnetic properties, is the CROVAC. The value of the tensile stress that came out from the tensile test was 700 MPa, that is high with respect to others SHMMs. Knowing the tensile stress, it was possible to design the rotor. The latter was carried out considering the high centrifugal forces involved, and considering valid the hypothesis of plane stress, the external diameter of the rotor was fixed to 35 mm. Subsequently, the rotor was built as laminated gluing 100 sheets of CROVAC.

At that point it was necessary to analyse the dynamic behaviour of the rotor. To do this, a 1-D FEM analysis for the study of rotodynamics was carried out. Since the rotor was attached to the shaft, the main problem was to determine the stiffness contribution of the rotor on the shaft. According to the hammering tests conducted on the free-free rotor, the best way to describe the stiffness contribution of the rotor was to increase the modulus of elasticity of the shaft in correspondence of rotor. In this way a model with a semi-structural mass was obtained. Then, the spacer and other bearing were added to the validated model. In particular, the spacer and the bearings were modelled, respectively, as non-structural and concentrated mass. Also in this case the model was successfully validated with an hammering test.

Once the free-free rotor was validated, a study of the supports was necessary in order to analyse the rotordynamic of the shaft. The supports were O-Rings made with

NBR-70, a viscoelastic material that had a stiffness and damping capability variables with the excitation frequency. Stiffness and damping of the O-Rings was found using a data-driven model found in literature. However, this is a non-linear model, so it cannot be used in frequency analysis. For this reason the O-Rings dynamic was described with a Maxwell-Weichert's model. The parameters were identified on the basis of the data-driven model with a Genetic Algorithm aimed to look for the optimal value that minimizes the difference between the data-driven model and the Maxwell-Weichert's model results. The Genetic Algorithm reached the convergence with few generations and the extrapolated results were very close to the non-linear model results.

At that point the Maxwell-Weichert's model and the rotor model were coupled and a rotordynamic analysis was performed. The model showed the presence of two critical speeds in the working range, however the unbalance response exhibited that the damping given by the O-Rings is sufficient to damp the rotor response, in fact the rotor passed through the critical speeds with a maximum displacement of 5 μm. This demonstrated the possibility of using the O-Rings for damping the vibrations of the rotor.

Given the good results obtained by the FEM model, experimental tests at high rotational speed were carried out. To perform the tests at high speed, it was necessary to lubricate the bearings. This was done with an oil-air system, as suggested with SKF technicians. This system allowed to reduce the friction looses in high speed bearings. During the operation of the rotor an accelerometer acquired the vibrations due to the unbalance and allowed the acquisition of a waterfall diagram. A first test was done with the non-balanced rotor, it was possible to reach 80000 rpm and to find that the first critical speed is very closed to the analytical one. So it was necessary to perform the rotor balancing before trying to reach 150000 rpm. Because of the small size of the rotor, it was very difficult to add mass, therefore the process of static and dynamic balancing was carried out by removing mass. To avoid removing mass from the rotor two discs were designed for this process. This allowed avoiding embrittlement and reductions in the performance of the electric motor. A second test with the balanced rotor wasn't performed since a firmware upgrade of the inverter limited the speed that can be reached in sensorless operation at 599 Hz.

The prototype ability to achieve high rotation speeds, without structural damage, were experimentally demonstrated. In fact, the CROVAC showed a higher tensile strength than others SHMMs and this allowed the hysteresis machine to operate at high angular speed without structural damage. Moreover, the numerical results show that the rotor passed through the critical speed well, and this should allow to reach the target speed of 150000 rpm. This demonstrated that the rotor response was sufficiently damped, so the O-Rings were a valid solution for introducing non-rotating damping. The validity of the numerical model is experimentally demonstrated since the first critical speed is very close to the real one. This confirms that the hysteresis electric machine is a valid solution for electric turbo-compound.

Finally, this thesis contributed to the realization of the experimental tests at high speed, preventing issues like huge vibrations, linked with rotordynamic, and rotor failure due to high centrifugal forces.

5.1 Future works

In future works, the target rotational speed of 150000 rpm has to be reached, to do this the issues linked to the inverter must be solved.

In order to pass from this simple prototype of a hysteresis machine to a complete turbo-compound model with impellers, some points must be analysed. Firstly, an analysis of the effect that the impellers have on rotordynamic must be carried out.

In addition, the dynamics of the O-Rings at high temperatures will have to be analysed, as they are very sensitive to the working temperature. The strength and reliability of high temperature materials will also need to be analyzed to avoid reliability problems.

In order to increase the hysteresis machine performance and implement the generator function, some analysis on the control strategies must be carried out.

Bibliography

[1] Press Service. Eu Parliament backs new CO2 emissions limits for cars and vans. pages 27–29, 2019.

[2] Fabio Chiara and Marcello Canova. A review of energy consumption, management, and recovery in automotive systems, with considerations of future trends. *Proceedings of the Institution of Mechanical Engineers, Part D: Journal of Automobile Engineering*, 227(6):914–936, 2013.

[3] Lauri Kütt and Matti Lehtonen. Automotive waste heat harvesting for electricity generation using thermoelectric systems—an overview. In *2015 IEEE 5th International Conference on Power Engineering, Energy and Electrical Drives (POWERENG)*, pages 55–62. IEEE, 2015.

[4] Zhang Jin-qiu, Peng Zhi-zhao, Zhang Lei, and Zhang Yu. A review on energy-regenerative suspension systems for vehicles. In *Proceedings of the world congress on engineering*, volume 3, pages 3–5, 2013.

[5] SR Cikanek and KE Bailey. Regenerative braking system for a hybrid electric vehicle. In *Proceedings of the 2002 American Control Conference (IEEE Cat. No. CH37301)*, volume 4, pages 3129–3134. IEEE, 2002.

[6] Ilya Kolmanovsky and Anna G Stefanopoulou. Evaluation of turbocharger power assist system using optimal control techniques. *SAE transactions*, pages 518–528, 2000.

[7] M Michon, SD Calverley, RE Clark, D Howe, JDA Chambers, PA Sykes, PG Dickinson, M Mc Clelland, G Johnstone, R Quinn, et al. Modelling and testing of a turbo-generator system for exhaust gas energy recovery. In *2007 IEEE Vehicle Power and Propulsion Conference*, pages 544–550. IEEE, 2007.

[8] `https://www.garrettmotion.com/news/media/press-release/garrett-to-launch-industrys-first-electric-turbo/`.

[9] Renato Galluzzi, Andrea Tonoli, and Nicola Amati. Magnetic hysteresis machines for next-generation electric turbochargers. In *2017 International Conference of Electrical and Electronic Technologies for Automotive*, pages 1–5. IEEE, 2017.

[10] Aleksandar Borisavljevic, Henk Polinder, and Jan Abraham Ferreira. On the speed limits of permanent-magnet machines. *IEEE Transactions on Industrial Electronics*, 57(1):220–227, 2009.

[11] JR Bumby, ES Spooner, J Carter, H Tennant, G Ganio Mego, G Dellora, W Gstrein, H Sutter, and J Wagner. Electrical machines for use in electrically assisted turbochargers. In *Second International Conference on Power Electronics, Machines and Drives (PEMD 2004).*, volume 1, pages 344–349. IET, 2004.

[12] Federico Millo, Fabio Mallamo, E Pautasso, and G Ganio Mego. The potential of electric exhaust gas turbocharging for hd diesel engines. Technical report, SAE Technical paper, 2006.

[13] David Gerada, Abdeslam Mebarki, Neil L Brown, Keith J Bradley, and Chris Gerada. Design aspects of high-speed high-power-density laminated-rotor induction machines. *IEEE Transactions on Industrial Electronics*, 58(9):4039–4047, 2010.

[14] Melanie Michon, Stuart D Calverley, Richard E Clark, David Howe, Mike McClelland, and Paul Sykes. Switched reluctance turbo-generator for exhaust gas energy recovery. In *2006 12th International Power Electronics and Motion Control Conference*, pages 1801–1807. IEEE, 2006.

[15] Stuart David Calverley, GW Jewell, and RJ Saunders. Design of a high speed switched reluctance machine for automotive turbo-generator applications. *SAE transactions*, pages 3246–3255, 1999.

[16] JJ Nitao, ET Scharlemann, and BA Kirkendall. Equivalent circuit modeling of hysteresis motors. Technical report, Lawrence Livermore National Lab.(LLNL), Livermore, CA (United States), 2009.

[17] Charles Proteus Steinmetz. *Theory and calculation of alternating current phenomena*, volume 4. McGraw-Hill Book Company, Incorporated, 1916.

[18] Renato Galluzzi, Nicola Amati, and Andrea Tonoli. Modeling, design and validation of magnetic hysteresis motors. *IEEE Transactions on Industrial Electronics*, 2019.

[19] Aldo Canova and Fabio Cavalli. Design procedure for hysteresis couplers. *IEEE Transactions on Magnetics*, 44(10):2381–2395, 2008.

[20] Giancarlo Genta. *Kinetic energy storage: theory and practice of advanced flywheel systems*. Butterworth-Heinemann, 2014.

[21] G Genta, C Delprete, and D Bassani. Dynrot: a finite element code for rotordynamic analysis based on complex co-ordinates. *Engineering Computations*, 13(6):86–109, 1996.

[22] Giancarlo Genta. *Dynamics of rotating systems*. Springer Science & Business Media, 2007.

[23] Jason D Ede, ZQ Zhu, and David Howe. Rotor resonances of high-speed permanent-magnet brushless machines. *IEEE Transactions on Industry Applications*, 38(6):1542–1548, 2002.

[24] Philipp Bättig and Jürg Schiffmann. Data-driven model for the dynamic characteristics of o-rings for gas bearing supported rotors. *Journal of Applied Mechanics*, 86(8):081003, 2019.

[25] Giancarlo Genta. *Vibration dynamics and control*. Springer, 2009.

[26] Angelo Bonfitto, Andrea Tonoli, and Nicola Amati. Viscoelastic dampers for rotors: Modeling and validation at component and system level. *Applied Sciences*, 7(11):1181, 2017.

[27] Johannes Kunz and Mario Studer. Determining the modulus of elasticity in compression via shore-a hardness. *Kunststoffe international*, 96(6):92–94, 2006.

[28] R Lewandowski, A Bartkowiak, and H Maciejewski. Dynamic analysis of frames with viscoelastic dampers: a comparison of damper models. *Structural Engineering and Mechanics*, 41(1):113–137, 2012.

[29] David B Fogel. An introduction to simulated evolutionary optimization. *IEEE transactions on neural networks*, 5(1):3–14, 1994.

[30] David E Goldberg. Genetic algorithms in search, optimization, and machine learning, addison wesley, reading, ma. *SUMMARY THE APPLICATIONS OF GA-GENETIC ALGORITHM FOR DEALING WITH SOME OPTIMAL CALCULATIONS IN ECONOMICS*, 1989.